

Article

Excellent Performance and Feasible Mechanism of ErO_x-Boosted MnO_x-Modified Biochars Derived from Sewage Sludge and Rice Straw for Formaldehyde Elimination: In Situ DRIFTS and DFT

Jiajie Wang^{1,2,3}, Lei Gao^{1,2,3,4,*}, Dong Xie^{2,3}, Caiting Li⁴, Liping Xiang^{2,3}, Yun Jiang^{1,2,3}, Qing Xu^{1,2,3}, Huiyu Xiong^{1,2,3}, Lei Yi^{1,2,3}, Jie Liu^{1,2,3} and Jiajun Wu^{1,2,3}

¹ School of Reces Environment and Safety Engineering, University of South China, Hengyang 421001, China; 13606648258@163.com (J.W.); 13357570708@163.com (Y.J.); 18552246909@163.com (Q.X.); xionghuiyuxue@163.com (H.X.); 15973617828@163.com (L.Y.); 16670968032@163.com (J.L.); 18230461231@163.com (J.W.)

² National & Local Joint Engineering Research Center for Airborne Pollutants Control and Radioactivity Protection in Buildings, Hengyang 421001, China; wwtf003620749@163.com (D.X.); 19818504851@163.com (L.X.)

³ Key Laboratory of Prefabricated Building Energy Saving Technology of Hunan Province, Hengyang 421001, China

⁴ College of Environmental Science and Engineering, Hunan University, Changsha 410082, China; wei2912323925@163.com

* Correspondence: 2019000032@usc.edu.cn; Tel.: +86-15274800478

Abstract: To avoid resource waste and environmental pollution, a chain of ErO_x-boosted MnO_x-modified biochars derived from rice straw and sewage sludge (Er_yMn_{1-y}/BACs, where biochars derived from rice straw and sewage sludge were defined as BACs) were manufactured for formaldehyde (HCHO) elimination. The optimal 15%Er_{0.5}Mn_{0.5}/BAC achieved a 97.2% HCHO removal efficiency at 220 °C and exhibited favorable E_{HCHO} and thermal stability in a wide temperature window between 180 and 380 °C. The curbed influences of H₂O and SO₂ offset the boosting effect of O₂ in a certain range. Er–Mn bimetallic-modified BACs offered a superior HCHO removal performance compared with that of BACs boosted using Er or Mn separately, owing to the synergistic effect of ErO_x and MnO_x conducive to improving the samples' total pore volume and surface area, surface active oxygen species, promoting redox ability, and inhibiting the crystallization of MnO_x. Moreover, the support's hierarchical porous structure not only expedited the diffusion and mass transfer of reactants and their products but also elevated the approachability of adsorption and catalytic sites. Notably, these prominent features were partly responsible for the outstanding performance and excellent tolerance to H₂O and SO₂. Using in situ DRIFTS characterization analysis, it could be inferred that the removal process of HCHO was HCHO_{ad} → dioxymethylene (DOM) → formate species → CO₂ + H₂O, further enhanced with reactive oxygen species. The DFT calculation once again proved the removal process of HCHO and the strengthening effect of Er doping. Furthermore, the optimal catalytic performance of 15%Er_{0.5}Mn_{0.5}/BAC demonstrated its vast potential for practical applications.

Keywords: HCHO; catalytic oxidation; Er–Mn oxides; density-functional theory; hierarchical porous biochar



Citation: Wang, J.; Gao, L.; Xie, D.; Li, C.; Xiang, L.; Jiang, Y.; Xu, Q.; Xiong, H.; Yi, L.; Liu, J.; et al. Excellent Performance and Feasible Mechanism of ErO_x-Boosted MnO_x-Modified Biochars Derived from Sewage Sludge and Rice Straw for Formaldehyde Elimination: In Situ DRIFTS and DFT. *Catalysts* **2023**, *13*, 1222. <https://doi.org/10.3390/catal13081222>

Academic Editor: John Vakros

Received: 6 July 2023

Revised: 3 August 2023

Accepted: 9 August 2023

Published: 17 August 2023



Copyright: © 2023 by the authors. Licensee MDPI, Basel, Switzerland. This article is an open access article distributed under the terms and conditions of the Creative Commons Attribution (CC BY) license (<https://creativecommons.org/licenses/by/4.0/>).

1. Introduction

The robust growth of industrial activities in China's now mammoth economy has led to a rapid increase in the demand for coal, one of the main energy sources. Volatile organic compounds (VOCs) discharged in large quantities from coal-fired power stations are mainly composed of aldehydes, alkanes and alkenes, and chlorinated hydrocarbons [1,2].

In addition to posing a significant threat to human health, these pollutants also generate gas pollution, forming photochemical smog and secondary organic aerosols that contribute to the dangerous depletion of stratospheric ozone [3]. In particular, as a common VOC, HCHO has been classified as a Class A carcinogen by the World Health Organization, and it is also widely recognized as a hazard to human health [4,5]. Consequently, researchers have developed efficient methods to remove HCHO, among which adsorption, photocatalysis, condensation, catalytic oxidation, biological filtration, and other technologies have recently emerged [6,7]. Among these technological endeavors, catalytic oxidation is regarded as an environmentally friendly, economical, and promising solution [7]. It is known that the performance of catalysts is vital for the efficiency of oxidation reactions. In the past several decades of research, supported noble metals and supported transition metal oxides have been considered key catalysts for the adsorption and catalytic oxidation of HCHO [7,8]. A series of metal oxide supports, including MnO_x , TiO_2 , CeO_2 , and FeO_x and their composites, such as $\text{MnO}_x\text{-CeO}_2$, $\text{CeO}_2\text{-Co}_3\text{O}_4$, and $\text{In}_2\text{O}_3\text{-SnO}_2$, have been used in a wide range of studies on catalytic HCHO due to their excellent redox effects, the high dispersity of the supported metal oxides, and the metal–support interactions (MSIs) between the supports and the supported metal oxides [9–11]. However, applications of these common metal oxide supports are restricted owing to certain disadvantages, such as irregular shapes, unsuitable sizes, uneven structures, and high prices [12,13]. Against this backdrop, despite their own problems, biochar supports hold potential for HCHO removal because of their low prices, adjustable sizes, large specific surface areas, excellent hydrophobicity, and rich sources [14]. Biochars' hydrophilic and porous structures provide them not only with excellent supports to convert VOCs into CO_2 and H_2O but also suitable mediums to remove a variety of gas pollutants, such as NO_x , SO_2 and Hg^0 [15–17]. Unlike most commercial activated carbon, hierarchical porous biochars are mainly composed of mesopores and macropores and not micropores, which significantly reduces the influence of internal diffusion and mass transfer on catalytic oxidation and adsorption rates [2,18]. In addition, mesopores and macropores can be used as spacious rooms for active ingredient dispersion, providing channels for the transfer and diffusion of other active substances, such as electrons [18]. Therefore, researching new types of efficient and cheap hierarchical porous biochars has become a focus in the field of catalysis.

Unfortunately, the finite number of surface functional groups and limited active sites in pristine biochars are insufficient to remove various VOCs. It has been reported that loading noble metals or transition metal oxides onto biochars could significantly enhance their catalytic activity and adsorption capacity [19]. Compared with noble metals, transition metal oxides provide lower costs and stronger resistance to poisoning, making them attractive alternatives to improve biochars' activity [20]. In particular, manganese oxides have become a major research topic because of their rapid electron transfer, abundant oxygen vacancies, and variable valences [21,22]. Notably, manganese oxides are regarded as a promising class of transition metal oxides, with relatively large oxygen storage capacities and high activity during the removal of VOCs [23]. Based on previous studies, Mn's different valence states from -3 to $+7$ allow its oxides to provide abundant reactive oxygen species while it also transfers activated electrons into a mobile electron environment that increases redox reactions [24].

However, manganese oxides are still limited by their low resistance to SO_2 poisoning, thermal instability, excessive by-products, and other problems in practical industrial applications [25]. To improve the anti- SO_2 performance of Mn-based catalysts, it has become a promising method to modify the catalysts with other metal elements to exploit the synergistic effect between bimetallic oxides [26]. As a rare earth metal, Er (erbium) has often been used in various fields in modified catalysts because it does not completely occupy the 4f and empty 5d orbitals. For example, adding a small amount of Er doping could significantly augment the oxygen vacancy concentration and oxygen storage capacity of CeZr/TiO_2 catalysts, generating excellent anti- SO_2 performance and SCR activity [27]. In addition, the presence of Er oxide in a $\text{YAlO}_3/\text{TiO}_2\text{-Fe}_2\text{O}_3$ composite created good acoustic

catalytic activity [26]. According to studies, Er and its composite oxides have been applied in a series of metal-oxide-supported catalysts, but they have rarely been applied in catalysts with biochars as the supports and for HCHO elimination [26–28]. For the above reasons, using ErO_x -boosted MnO_x -modified biochars to improve catalytic activity is encouraged, albeit a few reports on the utilization of such catalysts to remove VOCs in simulated flue gas and the catalytic oxidation mechanism of HCHO with $\text{Er}_y\text{Mn}_{1-y}/\text{BACs}$ are still unclear. To shed light on this, a range of $\text{Er}_y\text{Mn}_{1-y}/\text{BACs}$ samples were investigated for HCHO removal in this novel work, emphasizing three aspects: (1) the performance and practical application of $\text{Er}_y\text{Mn}_{1-y}/\text{BACs}$ catalysts for HCHO removal; (2) the mechanism of HCHO removal by $\text{Er}_y\text{Mn}_{1-y}/\text{BACs}$ catalysts; and (3) the physicochemical properties and structural features of these catalysts, aiming to explore the relationship between the physicochemical properties and catalytic performance of $\text{Er}_y\text{Mn}_{1-y}/\text{BACs}$ as well as to develop a new and efficient catalyst for HCHO removal.

2. Experimental Section

2.1. Sample Synthesis

Sewage sludge was collected from the Shuikoushan Industrial Sewage Treatment Plant, while rice straw was acquired from the outskirts of Hengyang City, Hunan Province, PR China. The biochars with sewage sludge, rice straw, and their combination as precursors were labeled as SAC, SAW, and BAC, respectively. The fabrication methods of the biochars have been described in detail in our past work [29]. The active ingredient precursors were manganese(II) acetate tetrahydrate or erbium(III) nitrate pentahydrate, while SAC, SAW, and BAC acted as the supports, in which the Mn- or Er oxide-modified catalysts were fabricated using the facile ultrasonic-assisted impregnation method. First, the desired precursors of erbium(III) nitrate pentahydrate or manganese(II) acetate tetrahydrate were uniformly dissolved in deionized water. Subsequently, the calculated amounts of the corresponding supports were impregnated in the precursor solutions for 25 h, undergoing ultrasonic sound treatment during the first 2 h. Lastly, the acquired samples were positioned in a drying oven until completely dried and then calcined at 450 °C for 5 h with constant N_2 protection. $\text{XEr}_y\text{Mn}_{1-y}/\text{BAC}$ catalysts were thus obtained, where X represents the mass fractions of the doping active metal oxides designated as 5%, 10%, 15%, and 20%. In addition, y and 1 – y represent the mole ratio of Er to Mn in the bimetallic oxides. 15%Er/BAC, 15%Mn/BAC, 15% $\text{Er}_{0.5}\text{Mn}_{0.5}$ /SAC, and 15% $\text{Er}_{0.5}\text{Mn}_{0.5}$ /SAW were also manufactured in the above manner.

2.2. Samples Characterization

First, a TriStarII3020 surface area porosity analysis tube (America Micromeritics, Georgia, GA, USA) was deployed to evaluate the pore parameters and specific surface areas of the samples. Scanning electron microscopy (SEM) photographs were obtained to analyze the surface morphologies and structures of the samples with a MIRA4 analyzer (TESCAN, Prague, Czech Republic). Transmission electron microscope (TEM) images were obtained with a Technai G2 F20 (FEI, Colombia MD USA) to view the samples' microstructures. Next, the X-ray diffraction (XRD) results of the components' dispersivity and crystallinity were obtained using a Bruker D8-Advance X-ray diffraction installation. H_2 temperature-programmed reduction (H_2 -TPR) was carried out using a Tianjin Xianquan TP-5080 automatic chemical adsorption instrument. The samples' chemical element states and chemical compositions were investigated with a Thermo ESCALAB 250XI X-ray photoelectron spectrometer (America Thermo, Lexington, MA, USA). Finally, in situ diffuse reflectance infrared Fourier-transform spectroscopy (DRIFTS) for the samples was conducted with a Nicolet iz10 (Thermo Fisher, Lexington, MA, USA).

2.3. Experimental Setup and Procedure

Figure 1 shows the device sketch for evaluating the HCHO elimination performance, which consisted of the following three main sectors. The first component was the simulated

flue gas supply system, where the simulative flue gas (SFG) contained 200.0 ± 2.0 ppm of HCHO, balanced N_2 , and 6% O_2 . Gaseous HCHO was prepared using a peristaltic pump to infuse a solution of 38 wt% HCHO into a polyethylene tube enclosed within a temperature-controlled heater. Moreover, the carrier gas of 80 mL/min N_2 carried the high-humidity gas-phase HCHO and passed through the condenser device to remove the gas-phase water vapor. The second component was a sustaining flow-fixed bed reactor. For each experiment, a 0.5 g sample was placed in a quartz tube (inner diameter = 10 mm; length = 1200 mm), and the total flow rate was maintained at 500 mL/min using a programmed heating tube furnace and various matching mass flow controllers, which corresponded to a gas hourly space velocity (GHSV) of approximately $64,000 \text{ h}^{-1}$. The corresponding gas components were plurally mixed before entering the fixed bed reactor. The third component was the gas analyzer system, which included a PGM7340 analyzer (RAE Systems, San Francisco, CA, USA) and a PGA-650 analyzer (Phymetrix, Medford, NY, USA) to survey the HCHO and CO_2 concentrations, respectively. The required HCHO concentration was regularly checked to maintain stability for at least 30 min before the start of the test. In addition, trial tests were performed before the experiment to lessen interference from the instrument and exterior elements.

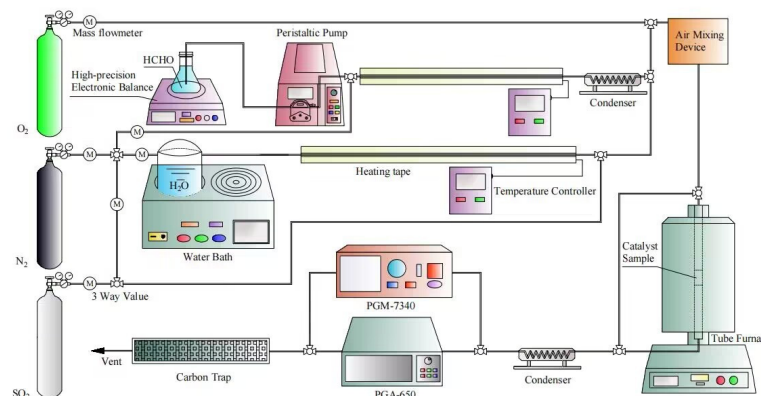


Figure 1. The apparatus diagram for HCHO removal.

The HCHO removal efficiency (E_{HCHO}) and CO_2 selectivity (S_C) were determined using the following formulae:

$$E_{\text{HCHO}} = \frac{[\text{HCHO}]_{\text{in}} - [\text{HCHO}]_{\text{out}}}{[\text{HCHO}]_{\text{in}}} \times 100\% \quad (1)$$

$$S_C = \frac{[\text{CO}_2]_{\text{out2}} - [\text{CO}_2]_{\text{out1}}}{[\text{HCHO}]_{\text{in}} - [\text{HCHO}]_{\text{out}}} \times 100\% \quad (2)$$

where the HCHO concentrations at the inlet and outlet are represented as $[\text{HCHO}]_{\text{in}}$ and $[\text{HCHO}]_{\text{out}}$, respectively. Similarly, the outlet CO_2 concentrations in the blank experiments and performance tests are denoted as $[\text{CO}_2]_{\text{out1}}$ and $[\text{CO}_2]_{\text{out2}}$. Furthermore, to reduce the error of the experiment, E_{HCHO} and S_C were taken as the average values of three parallel experiments.

3. Results and Discussion

3.1. Sample Characterization

3.1.1. BET Analysis

Table 1 overviews the physical properties of the primordial BAC and modified BACs, including total pore volumes, BET surface areas, and average pore diameters. Figure 2a depicts the N_2 adsorption/desorption isotherms of the samples. All the isotherms exhibit the typical IV with H3 hysteresis loops, revealing the existence of slit-shaped mesopores based on the IUPAC [30,31]. The primordial BAC exhibited the maximal BET surface area of $284.3071 \text{ m}^2/\text{g}$ and the highest total pore volume of $0.263 \text{ cm}^3/\text{g}$. Both the specific

surface areas and total pore volumes of the boosted samples decreased with the addition of the metal oxides. This might be due to sections of the existing pores being covered and destroyed by the loaded metal oxides [25]. The bimetallic-modified samples had higher specific surface areas than the mono-metallic-modified samples, and this phenomenon was attributed to the synergistic effect between Er and Mn oxides, which improves the dispersity of metal oxides [32,33]. The total pore volumes and specific surface areas of the $\text{Er}_{0.5}\text{Mn}_{0.5}/\text{BAC}$ samples decreased as a result of the increase in the loading value. This phenomenon might be because of the agglomeration of metal oxides, and the blocking of more voids by Er and Mn oxides becomes increasingly significant with the increasing metal oxide loading value [29,30]. Combining the subsequent SEM analysis and the experimental results in Comparison of Catalytic Performance, the specific surface area was not the exclusive determinant of the samples' activity. Furthermore, the samples' pore size distribution curves in Figure 2b show that the pore volume characteristics of the prepared samples were mainly determined by micropores and mesopores.

Table 1. The BET specific surface areas and pore parameters of primordial BAC and modified BACs.

Sample	BET Surface Area (m^2/g)	Total Pore Volume (cm^3/g)	Average Pore Diameter (nm)
Primordial BAC	284.3071	0.263	5.0651
5% $\text{Er}_{0.5}\text{Mn}_{0.5}/\text{BAC}$	240.2477	0.218	5.3080
10% $\text{Er}_{0.5}\text{Mn}_{0.5}/\text{BAC}$	204.4189	0.189	5.6334
15%Er/BAC	185.3815	0.189	5.8242
15%Mn/BAC	198.0249	0.196	5.7362
15% $\text{Er}_{0.5}\text{Mn}_{0.5}/\text{BAC}$	198.7038	0.180	4.9473
20% $\text{Er}_{0.5}\text{Mn}_{0.5}/\text{BAC}$	159.5359	0.154	5.2493

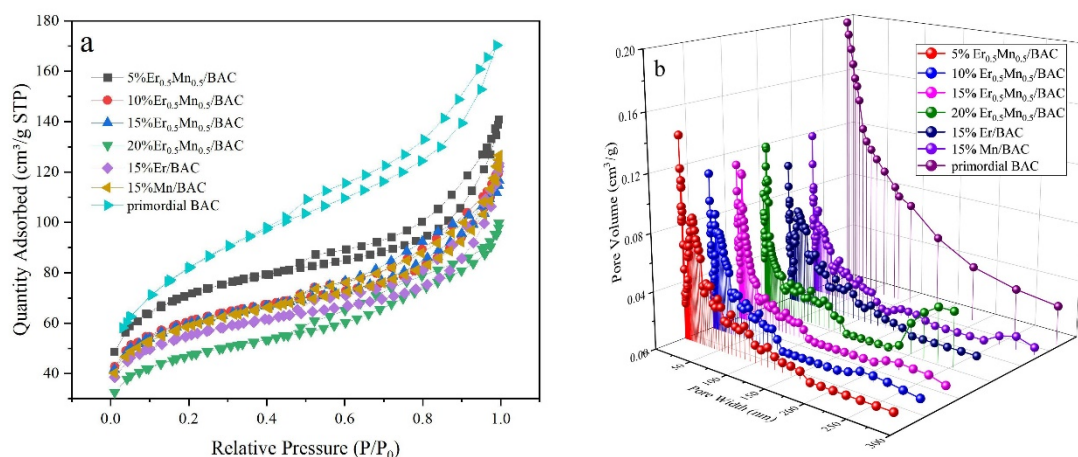


Figure 2. (a) Nitrogen adsorption and desorption isotherm curves; (b) BJH pore size distribution curves for primordial BAC and modified BACs.

3.1.2. SEM and TEM Analysis

The SEM images of the primordial BAC and modified BACs are shown in Figure 3. The surface morphology and structure of the primordial BAC dramatically changed after the import of metal oxides. As demonstrated in Figure 3b, only a few agglomerates located in 5% $\text{Er}_{0.5}\text{Mn}_{0.5}/\text{BAC}$ and most surfaces of 5% $\text{Er}_{0.5}\text{Mn}_{0.5}/\text{BAC}$ were not completely used, allowing further loading with additional metal oxides. For 10% $\text{Er}_{0.5}\text{Mn}_{0.5}/\text{BAC}$, while part of the effective area was fully utilized, some of the surface of 10% $\text{Er}_{0.5}\text{Mn}_{0.5}/\text{BAC}$ was not exploited. It was thought that more dispersed active metal oxides resulted in more adsorption or catalytic sites, thus improving catalytic activity [29,34]. Regarding 15% $\text{Er}_{0.5}\text{Mn}_{0.5}/\text{BAC}$, almost all surface areas were highly dispersed with metal oxides, with some agglomerating metal oxides and more agglomerates existing in 20% $\text{Er}_{0.5}\text{Mn}_{0.5}/\text{BAC}$.

Consequently, the excess metal oxides destroyed some pre-existing pores due to more serious agglomerates [35,36]. This appearance also dovetailed with the frontal BET results. Furthermore, as revealed in Figure 3f, EDX was used to detect the rough element ratio of Er to Mn in 15%Er_{0.5}Mn_{0.5}/BAC. The Mn/Er atomic ratio in a particular morphology of 15%Er_{0.5}Mn_{0.5}/BAC was 0.93, which is almost equal to the theoretical Mn/Er atomic ratio in 15%Er_{0.5}Mn_{0.5}/BAC (Mn/Er = 1). The experiments demonstrated that Er and Mn were equally dispersed in 15%Er_{0.5}Mn_{0.5}/BAC and that ErO_x was slightly more likely to agglomerate than MnO_x.

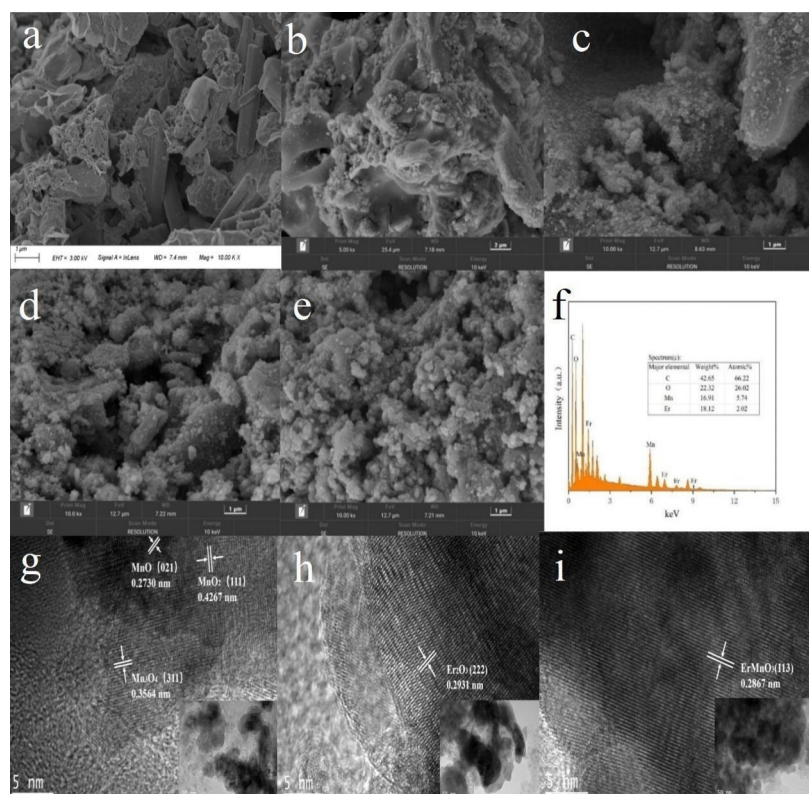


Figure 3. The SEM and TEM images of primordial BAC and modified BACs. (a) SEM image ($\times 10,000$) and (b–e) SEM images ($\times 20,000$): (a) primordial BAC, (b) 5%Er_{0.5}Mn_{0.5}/BAC, (c) 10%Er_{0.5}Mn_{0.5}/BAC, (d) 15%Er_{0.5}Mn_{0.5}/BAC, (e) 20%Er_{0.5}Mn_{0.5}/BAC, and (f) EDX image of 15%Er_{0.5}Mn_{0.5}/BAC. TEM images: (g) 15%Mn/BAC, (h) 15%Er/BAC, and (i) 15%Er_{0.5}Mn_{0.5}/BAC.

The TEM images of 15%Mn/BAC, 15%Er/BAC, and 15%Er_{0.5}Mn_{0.5}/BAC at 50 nm and 5 nm are revealed in Figure 3, where visible lattice fringes appeared on the crystal nanoparticles. Figure 3g reveals that the particle size of 15%Mn/BAC was approximately 20 nm, and three lattice stripes of 0.2730 nm, 0.4267 nm, and 0.3564 nm were detected, which can be attributed to the MnO (0 2 1) phase, MnO₂ (1 1 1) phase, and Mn₃O₄ (3 1 1) phase, respectively [25]. The particle size of 15%Er/BAC shown in Figure 3h was approximately 27 nm, and a lattice fringe of 0.2961 nm was determined to belong to the Er₂O₃ (2 2 2) phase. In addition, the particle size of 15%Er_{0.5}Mn_{0.5}/BAC shown in Figure 3i was approximately 19 nm, which was lesser than that of 15%Er/BAC and 15%Mn/BAC, hinting that the incorporation of Er reduced the crystallinity and particle sizes of Mn/BAC to a certain extent, as only one lattice fringe of 0.2877 nm corresponding to ErMnO₃ (1 1 3) phases was observed. Moreover, the absence of lattice streaks matching other metallic components also proved that the Er and Mn species existed as amorphous species [37]. The 5 nm and 50 nm TEM images clearly show that the Er and Mn species were highly decentralized in 15%Er_{0.5}Mn_{0.5}/BAC or emerged as amorphous species.

3.1.3. H₂-TPR Analysis

The redox reactions of the primordial BAC and modified BACs were analyzed using H₂-TPR. As elucidated in Figure 4, the two overlapping peaks occurred at approximately 652 °C and 718 °C in the primordial BAC, and the peak centered at 652 °C might be due to the reduction in adsorbed oxygen on the surface, while the latter could be attributed to the gasification of the BAC [37]. The peaks at these two positions in the other modified BAC samples were due to the same cause. An additional peak for 15%Er/BAC appeared at 538 °C, possibly as a result of Er₂O₃ participating in the redox reactions with the transformation into metallic erbium [38]. In addition, the first peak for 15%Mn/BAC at 417 °C can be ascribed to the reduction of MnO₂–Mn₂O₃/Mn₃O₄ and the second peak at 505 °C to the succedent reduction of Mn₃O₄–MnO [39,40]. Furthermore, three extra peaks were observed for 15%Er_{0.5}Mn_{0.5}/BAC. The two peaks below 500 °C were interpreted as being associated with the concurrent reduction of MnO₂/Mn₂O₃ to Mn₃O₄ and Er₂O₃ to Er, while the peak at approximately 540 °C might be associated with the conversion of Mn₃O₄ to MnO [41].

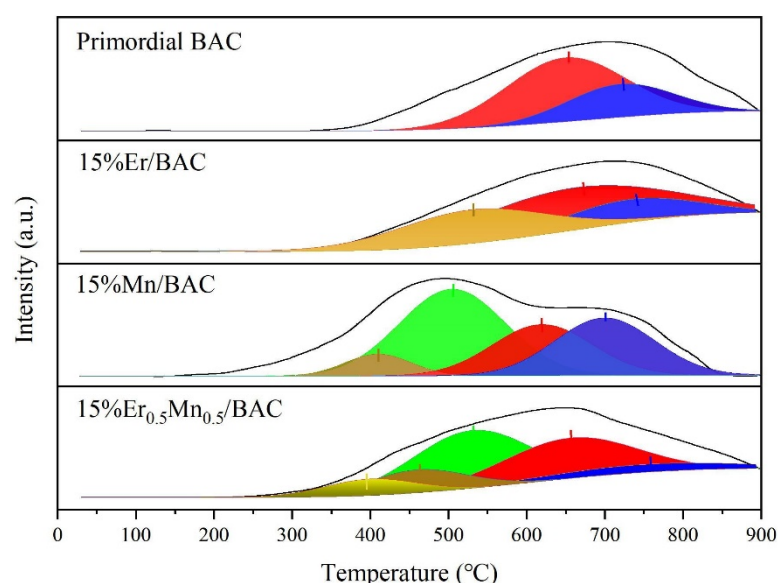


Figure 4. H₂-TPR profiles of primordial BAC and modified BACs.

It was shown that in comparison with 15%Er/BAC and 15%Mn/BAC, the corresponding two reduction peaks of 15%Er_{0.5}Mn_{0.5}/BAC were at lower temperatures and showcased better redox abilities [26,41]. This could be due to the following two reasons. A synergistic effect occurred between ErO_x and MnO_x, which might have led to structural deformation and surface oxygen defects, thus favoring catalytic oxidation reactions [42]. Second, the Mn⁴⁺/Mn³⁺ and Er³⁺/Er pairs expedited one another to form more surface oxygen vacancies, significantly accelerating reactant activation or increasing oxygen mobility [30,43]. Moreover, studies indicate that the inclusion of Er could enhance the low-temperature redox capacity of a catalyst, which is consistent with the results of these experiments. Therefore, this could explain why 15%Er_{0.5}Mn_{0.5}/BAC possessed outstanding catalytic activity at a lower temperature range [26,44].

3.1.4. XRD Analysis

XRD measurements were performed to probe into the crystal structures and chemical compositions of the primordial BAC and modified BACs, with the results displayed in Figure 5. Regarding the primordial BAC, nine diffraction peaks at $2\theta = 26.60^\circ$, 28.90° , 32.22° , 35.51° , 36.04° , 39.46° , 44.46° , 47.35° , and 56.10° were observed, wherein the peaks at $2\theta = 26.60^\circ$ and 44.46° were associated with the carbon matrix, while the other peaks at $2\theta = 28.9^\circ$, 32.22° , 35.51° , 36.04° , 39.46° , 47.35° , and 56.10° were ascribed to the presence of SiO₂ [25,37,42]. Interestingly, the peaks belonging to C and SiO₂ receded or disappeared

with the introduction of erbium oxides or manganese oxides, demonstrating that the external structures of the supports were violently changed via the loading of the active metal oxides [37]. Moreover, this phenomenon also indicated a strong interaction between these oxides and the supports [37,45]. Regarding 15%Er/BAC, five peaks at $2\theta = 20.6^\circ$, 40.1° , 47.2° , 56.5° , and 59.4° belonged to Er_2O_3 [46]. As for 15%Mn/BAC, four peaks at $2\theta = 40.55^\circ$, 59.84° , 69.50° , and 73.80° were clearly observed, in which the peaks at $2\theta = 59.84^\circ$ and 73.8° corresponded to Mn_3O_4 , and the peak at $2\theta = 40.55^\circ$ indicated the presence of MnO , whereas the peak at $2\theta = 69.5^\circ$ was assigned to MnO_2 . This phenomenon might be because different Mn species coexisted in these samples, showing faultless crystalline structures and distinct diffraction peaks. However, unlike 15%Er/BAC and 15%Mn/BAC, several characteristic peaks appeared in $\text{xEr}_{0.5}\text{Mn}_{0.5}/\text{BACs}$ at $2\theta = 47.16^\circ$, which were similar to ErMnO_3 [47]. Since the radii of Er^{3+} (0.881 Å) are close to those of Mn^{4+} (0.60 Å) and Mn^{3+} (0.66 Å), Er ions might dissolve in the MnO_2 lattice [48]. Significantly, in comparison with 15%Mn/BAC and 15%Er/BAC, the interrelated peaks delegating the interaction between Er and Mn were broader and weaker in 15% $\text{Er}_{0.5}\text{Mn}_{0.5}/\text{BAC}$, indicating that they favored the generation of fewer amorphous surface species, which could have increased the dispersion of the metal oxides and accelerated surface oxygen vacancies, improving the catalytic performance of the samples [43].

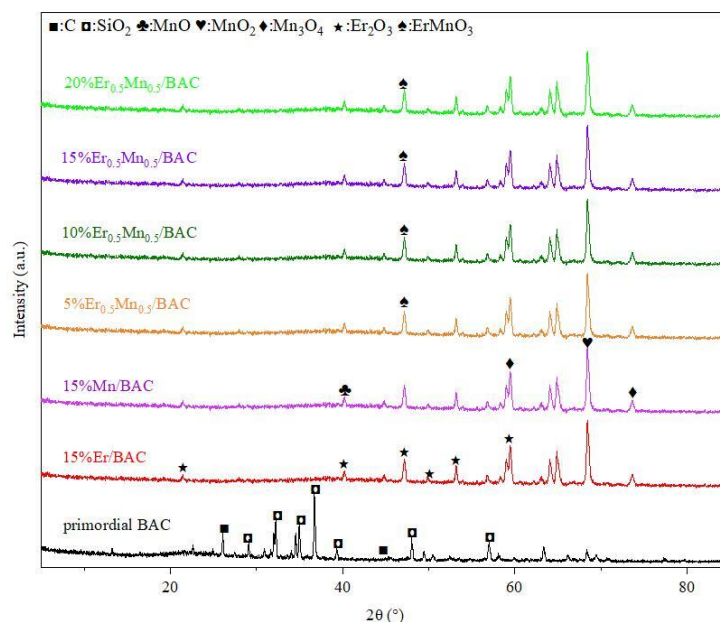


Figure 5. XRD patterns of primordial BAC and modified BACs.

3.1.5. XPS Analysis

XPS analysis was carried out on the primordial BAC and modified BAC samples to obtain information on the valence states and chemical compositions of the relevant elements. Figure 6a exhibits the three sub-peaks of the O 1s XPS spectra in these samples, where the peaks with lower binding energy values at 528.2–528.7 eV corresponded to lattice oxygen (O_α) and the peaks at approximately 529.7–530.1 eV were due to faintly bonded oxygen or chemisorbed oxygen (O_β), while the peaks at approximately 530.9–531.7 eV resulted from adsorbed water species (O_s) [49,50]. The primordial BAC lacked O_α , an oxygen reservoir, and the metal oxide modification favored O_α formation, thus enhancing the catalytic activity [32]. According to the SEM analysis, the metal oxides covered the surfaces of the samples in the loading and calcination stages, blocking the pre-existing type of oxygen, which offers a possible explanation for its disappearance. In addition, O_β exhibited extremely high reactivity and fluidity in the catalytic oxidation reaction, demonstrating the distinguished catalytic activity of removing HCHO [37,40]. Compared with the unsalted 15% $\text{Er}_{0.5}\text{Mn}_{0.5}/\text{BAC}$, the O_s ratio of used 15% $\text{Er}_{0.5}\text{Mn}_{0.5}/\text{BAC}$ increased from 16.46% to

38.26%, while that of O_{α} and O_{β} of used 15%Er_{0.5}Mn_{0.5}/BAC decreased from 38.33% and 45.21% to 34.76% and 26.98%, respectively, demonstrating the participation of O_{α} and O_{β} in the catalytic oxidation reactions [51]. Therefore, it can be inferred that more reactive oxygen species were conducive to accelerating the catalytic activity of HCHO removal.

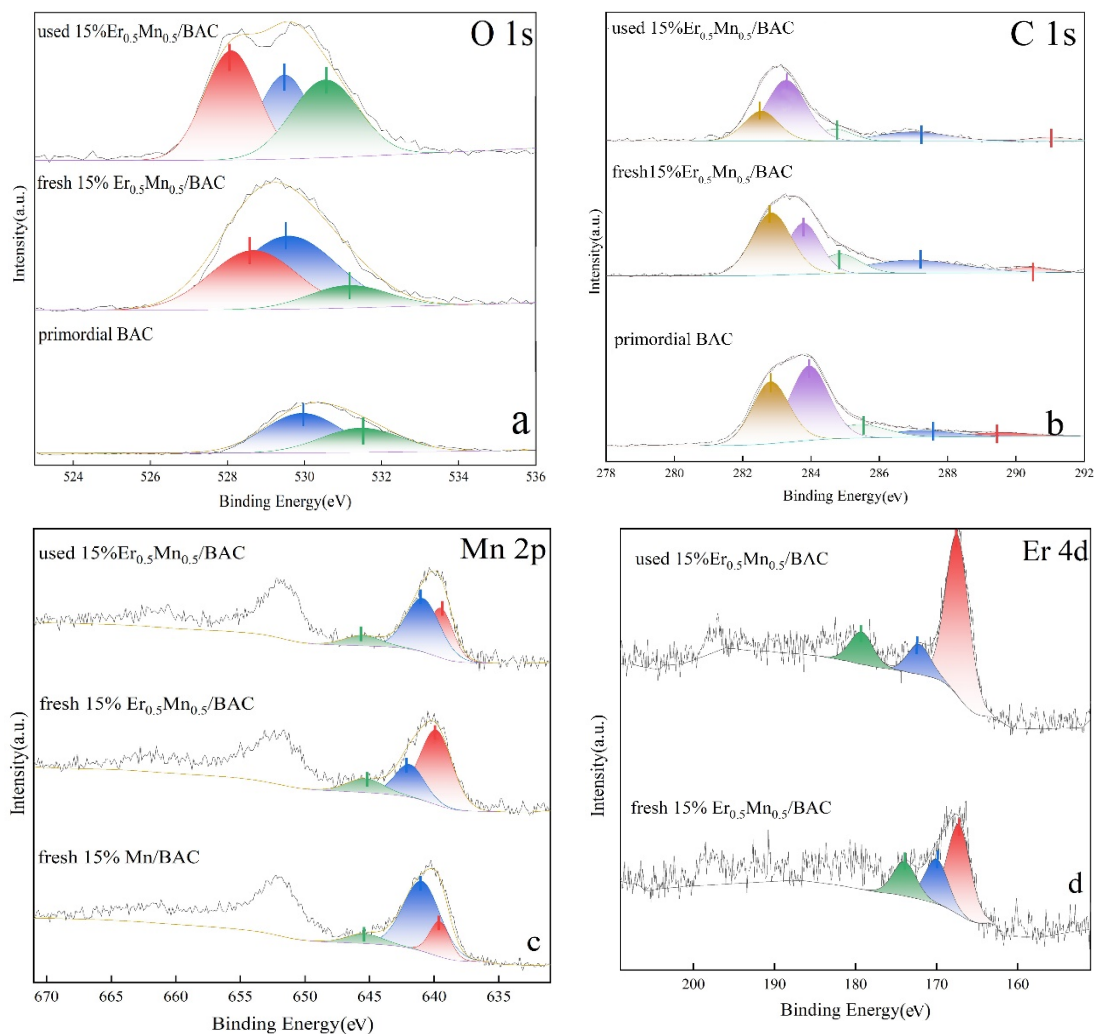


Figure 6. The XPS analysis of O 1s (a), C 1s (b), Er 4d (c), and Mn 2p (d) for primordial BAC, fresh 15%Mn/BAC, fresh 15%Er_{0.5}Mn_{0.5}/BAC, and used 15%Er_{0.5}Mn_{0.5}/BAC.

Figure 6b showcases the five sub-peaks of the C 1s XPS spectra, among which the generated characteristic peaks located at 282.5–282.9 eV, 283.8–284.2 eV, 284.9–285.8 eV, 287.3–287.8 eV, and 289.6–290.8 eV were related to graphitic carbon, carbon existing in alcohol or phenolic, carbonyl groups, carboxyl, or ester groups, and π - π^* transitions in aromatic rings, respectively [9,52]. In addition, the loading of metal oxides resulted in a boom in the ratio of COOH to C–C, which likely resulted from the impregnation of acetate or nitrate precursor solutions, where the decrease in C–O could be attributed to the desorption of chemisorbed oxygen via high-temperature calcination under the N₂ atmosphere [9]. In the modified BACs, the proportion of functional C–O groups decreased and the proportion of total-oxygen-containing functional groups heightened after the reactions, which was a possible outcome of the oxidation of C–O by reactive oxygen species during the removal of HCHO [53].

The Mn 2p XPS spectra are revealed in Figure 6c, and the main finding is that the three peaks were located at 638.5–639.2 eV, 641.2–642.4 eV, and 645.1–646.3 eV, corresponding to Mn²⁺, Mn³⁺, and Mn⁴⁺, respectively [36,54]. This intimated that Mn existed in three valence conditions, Mn²⁺, Mn³⁺, and Mn⁴⁺, during the entire reaction process, where the

sum of $\text{Mn}^{2+} + \text{Mn}^{3+} + \text{Mn}^{4+}$ can be defined as Mn^{n+} . In addition, the proportions of Mn^{2+} , Mn^{3+} , Mn^{4+} , and $\text{Mn}^{3+} + \text{Mn}^{4+}$ were calculated using $\text{Mn}^{2+}/\text{Mn}^{n+}$, $\text{Mn}^{3+}/\text{Mn}^{n+}$, $\text{Mn}^{4+}/\text{Mn}^{n+}$, and $\text{Mn}^{3+} + \text{Mn}^{4+}/\text{Mn}^{n+}$. In comparison with fresh 15%Mn/BAC, the proportions of $\text{Mn}^{4+}/\text{Mn}^{3+}$, $\text{Mn}^{4+} + \text{Mn}^{3+}$, and Mn^{4+} in fresh 15%Er_{0.5}Mn_{0.5}/BAC all increased to different degrees, signaling that the incorporation of ErO_x could expedite the increase in the Mn valence state and proving that redox reactions occurred between ErO_x and MnO_x. High-valence Mn, such as Mn^{4+} , participating in the redox cycle might help improve the catalytic activity of the sample and accelerate the removal of HCHO [55]. In addition, the proportions of $\text{Mn}^{4+}/\text{Mn}^{3+}$, $\text{Mn}^{4+} + \text{Mn}^{3+}$, and Mn^{4+} demonstrated a decreasing trend after the reactions, suggesting that Mn in the high-price state changed to a low-price state during the reactions.

Figure 6d shows the Er 4d XPS spectra, wherein three peaks could be observed at 167.1–168.3 eV, 169.1–171.2 eV, and 173.6–178.2 eV. The first peak corresponded to Er 4d5/2, indicating that Er existed in the modality of Er₂O₃ and, thus, in the state of Er³⁺ occurring at this time, while the last peak had a higher peak binding energy at 173.6–178.2 eV corresponding to Er 4d3/2, which could be a result of the Er metal oxides [38,56,57]. The peak in the middle indicated that the metal Er was first oxidized to Er²⁺, but because of the relatively unstable electronic configuration, it was rapidly oxidized to Er³⁺ [56]. Therefore, these values demonstrate that Er was successfully loaded onto the BAC samples and participated in the catalytic oxidation reaction in the Er³⁺ mode. Such binding energy values of Er 4d are consistent with those in perovskites [36]. All these phenomena testify that at least part of the Er₂O₃ transformed into the perovskite-like structure of ErMnO₃, which is consistent with the H₂-TPR analysis. This suggests that the addition of ErO_x could change the morphological structure of the catalyst.

3.2. Comparison of Catalytic Performance

3.2.1. Effect of Molar Ratio of Er/Mn

The performances of the 15%ErMn/BAC samples with diverse molar ratios of Er/Mn for HCHO elimination at 100–380 °C are listed in Figure 7. A roughly similar trend was observed in the E_{HCHO} of these samples. The E_{HCHO} first showed noticeable growth with the rise in the reaction temperature from 100 °C to 220 °C and subsequently behaved in a slight downward trend with the continuous enhancement of the reaction temperature at 220–380 °C. The former finding can be interpreted as the increase in the reaction temperature providing more kinetic energy and facilitating the chemical adsorption and oxidation of HCHO [58]. Meanwhile, the decline in the E_{HCHO} at excessively high temperatures could be caused by various reasons, such as the high temperatures inhibiting the physical adsorption of HCHO [37,59]. Another reason was the destruction of the BAC structure at high temperatures. In addition, vibrant metal oxides could catalytically oxidize the carbon matrix into H₂O and CO₂ [25]. Moreover, it was found that the E_{HCHO} of 15%Er_{0.5}Mn_{0.5}/BAC engendered the most outstanding performance in the 100–380 °C temperature range when the molar ratio of Er/Mn was 1:1. This optimal performance could be connected with the strongest synergistic effect between the two metal oxides with an appropriate molar ratio of Er/Mn [60,61]. Ultimately, 15%Er_{0.5}Mn_{0.5}/BAC showed the most outstanding performance at 220 °C in these samples, and its E_{HCHO} content was 97.2%.

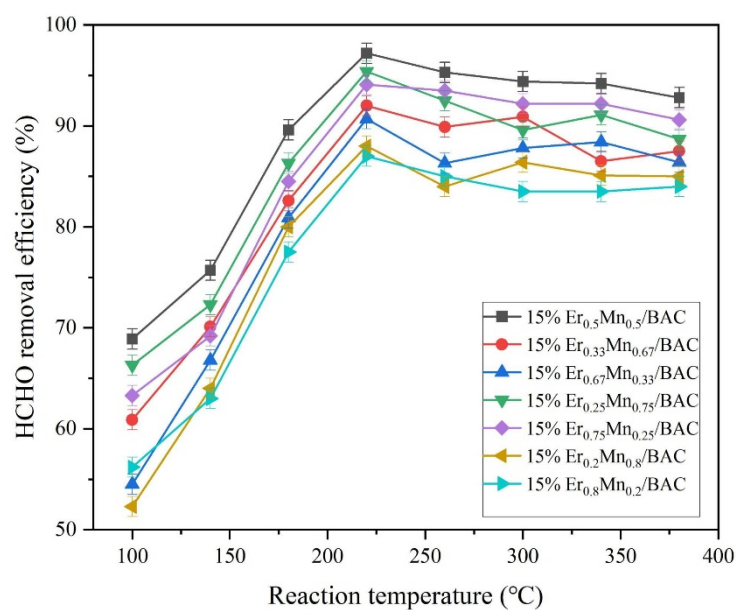


Figure 7. Effect of molar ratio of Er/Mn on HCHO removal in modified BACs. Reaction conditions: 200 ppm HCHO, 6% O₂, N₂ as balance gas, and T = 100–380 °C.

3.2.2. Effects of Support Materials

The support materials derived from diverse raw materials showed distinctive surface functional groups and intrinsic pore structures in different proportions of micropores, mesopores, and macropores, which directly influenced the mass transfer and pervasion of reactants and product molecules, thus playing an imperative role in the catalytic reactions [12,62]. Figure 8 showcases the effects of the support materials from diverse precursors on HCHO removal at an identical loading and molar ratio of metal oxides at 100–380 °C. Throughout the entire heating process, 15%Er_{0.5}Mn_{0.5}/BAC exhibited a better E_{HCHO} than 15%Er_{0.5}Mn_{0.5}/SAC and 15%Er_{0.5}Mn_{0.5}/SAW, which could be theoretically ascribed to 15%Er_{0.5}Mn_{0.5}/BAC neutralizing 15%Er_{0.5}Mn_{0.5}/SAW and 15%Er_{0.5}Mn_{0.5}/SAC. It is conceivable that the hierarchical porous structure of 15%Er_{0.5}Mn_{0.5}/BAC well regulated the proportions of micropores, mesopores, and macropores via the BAC support, which was more conducive to the mass transfer and diffusion of reactant and offspring molecules [31]. In addition, the E_{HCHO} of 15%Er_{0.5}Mn_{0.5}/BAC and 15%Er_{0.5}Mn_{0.5}/SAW presented a decreasing trend with the increase in the reaction temperature at 220 and 300 °C, and 15%Er_{0.5}Mn_{0.5}/BAC's E_{HCHO} dropped lower than 15%Er_{0.5}Mn_{0.5}/SAW's at high temperatures. This may have been caused by high temperatures destroying the active centers and pore structures of BAC and SAW, and the thermal stability of BAC was higher than that of SAW [62,63]. In contrast, according to the BET analysis, 15%Er_{0.5}Mn_{0.5}/BAC possessed better physicochemical characteristics, which were conducive to the diffusion and mass transfer of gas reactants, and exhibited the best HCHO abatement performance across the entire temperature range.

3.2.3. Effects of Active Ingredients

The active ingredients and their loading values exerted important effects on the dispersion, aggregation, crystallization, and redox properties of the correlative metal oxides, which were closely related to the catalytic activities of the samples [39]. Figure 9a displays the effects of various ingredients on HCHO elimination in the primordial BAC and bimetallic-modified BAC samples with different loading values. It can be seen that the E_{HCHO} of the modified BAC samples first showed a significant upward trend with the increase in the loading value and then exhibited a slight downward trend with the excessive loading of metal oxides. The former could be attributed to the uniform dispersion of the loaded metal oxides on the sample surfaces, providing a large number of adsorption

or catalytic active sites, while the latter might be due to the more severe agglomeration caused by excess metal oxides, thus hiding voids and adsorption or catalytic activity sites. In addition, the E_{HCHO} of $X\text{Er}_{0.5}\text{Mn}_{0.5}/\text{BACs}$ increased continuously until the temperature reached 220 °C and dropped slightly as the reaction temperature increased further. 15% $\text{Er}_{0.5}\text{Mn}_{0.5}/\text{BAC}$ showed the highest catalytic activity of 97.2% at 220 °C and consistently demonstrated the best performance throughout the phase, which was likely a consequence of the better dispersion of the Er and Mn oxides, more oxygen vacancies, and the preeminent properties of the prepared sample. The SEM results also confirmed the superior physical and chemical properties of 15% $\text{Er}_{0.5}\text{Mn}_{0.5}/\text{BAC}$. Considering the metal oxide loading value as a significant influencing factor for HCHO removal, 15% $\text{Er}_{0.5}\text{Mn}_{0.5}/\text{BAC}$ was selected for a follow-up study in this work.

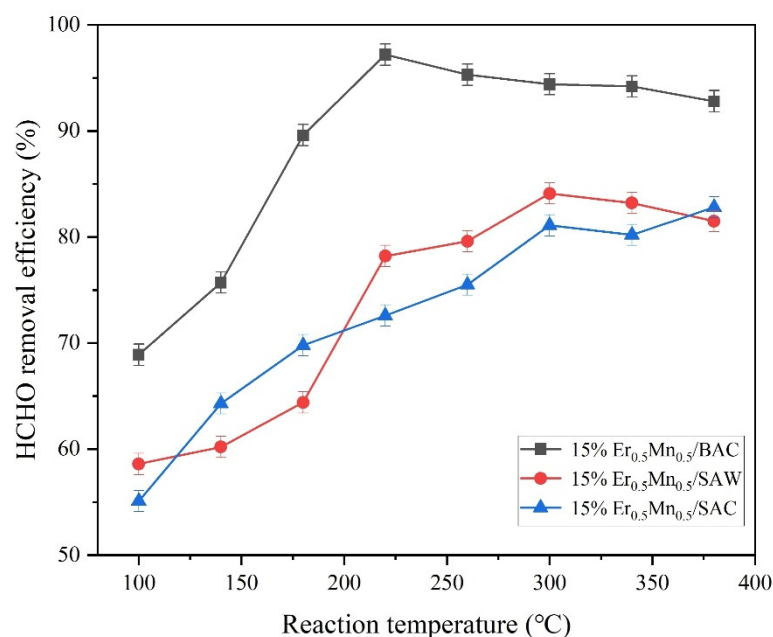


Figure 8. Effect of disparate support materials on HCHO removal.

As illustrated in Figure 9b, the E_{HCHO} of the Er- or Mn-modified samples demonstrated significant improvement compared with the primordial BAC. It was observed that the metal oxide loading greatly facilitated HCHO removal. 15% $\text{Er}_{0.5}\text{Mn}_{0.5}/\text{BAC}$ demonstrated superior performance and a wider effective temperature range than that of single-loading samples. The synergistic effect of the bimetallic oxides was the main factor behind the enhancement in the bimetallic oxides' dispersity, the number of oxygen vacancies, surface active substances, and the redox ability [39,64].

It was clear that the reaction temperature was a key factor in the catalytic reactions for a given catalyst, and the corresponding active temperature range always behaved similarly. Before this, the catalytic activity was proportional to the temperature rise due to an increase in the catalytic activation energy [17]. There might be several reasons why the E_{HCHO} decreased at high temperatures. Firstly, high temperatures can hamper the adsorption of reactant molecules [65]. Secondly, the catalytic oxidation of the carbon matrix by metal oxides leads to the structural destruction of the BAC [34,66].

3.3. Effect of Atmospheric Conditions

3.3.1. Effect of O_2

As an indispensable gas component in the actual flue gas, O_2 significantly influenced the conversion of reactive oxygen species associated with the catalytic oxidation procedures of HCHO [12,32]. Figure 10 displays the influences of O_2 concentrations on HCHO elimination in 15% $\text{Er}_{0.5}\text{Mn}_{0.5}/\text{BAC}$ at 220 °C. It was recognized that oxygen deficiency might impact the catalytic properties of the samples. Nevertheless, with a short supply

of oxygen, 15%Er_{0.5}Mn_{0.5}/BAC performed relatively well in terms of the E_{HCHO} due to the pre-existing lattice oxygen and chemisorbed oxygen both participating in the catalytic oxidation of HCHO [32,37]. XPS analysis demonstrated that residual O_α and O_β were on the surface of 15%Er_{0.5}Mn_{0.5}/BAC in a dearth of oxygen, which played a role in the catalytic oxidation of HCHO. Moreover, the E_{HCHO} significantly increased when the oxygen content was raised to 3%, but the variation in the E_{HCHO} was almost negligible as the O₂ concentration increased further. Ample gaseous oxygen to supplement the consumed O_α and O_β was essential for achieving an efficient HCHO removal performance [32,67]. Meanwhile, the oxygen vacancy and lattice defects on the surface of 15%Er_{0.5}Mn_{0.5}/BAC were conducive to the capture and transmission of O₂, thus further facilitating HCHO removal [68,69]. The above phenomenon demonstrated that only 3% oxygen could result in a significant enhancement in HCHO removal, and the oxygen content in the industrial flue gas was generally greater than that, thus well fulfilling this requirement.

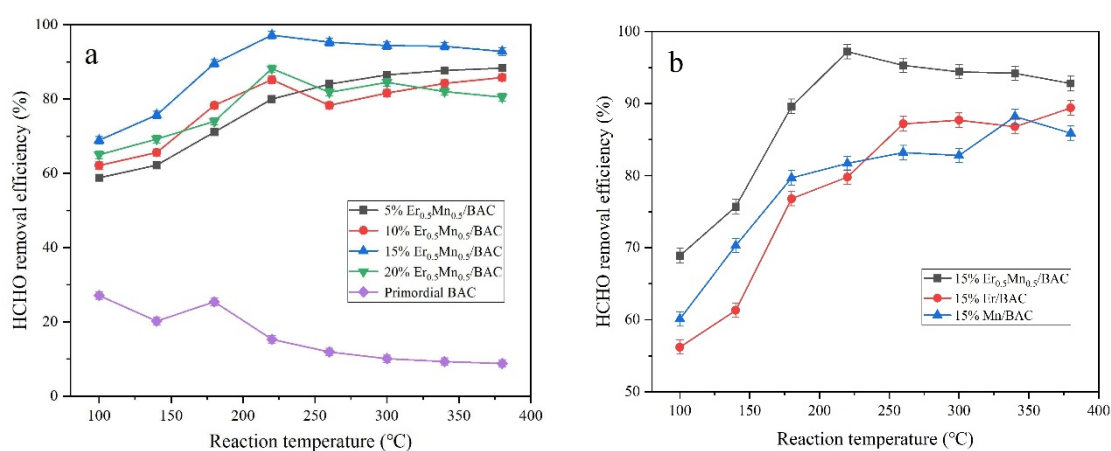


Figure 9. Effects of active ingredients on HCHO removal in primordial BAC and modified BACs. (a) The performance of HCHO removal in 5–20%Er_{0.5}Mn_{0.5}/BACs; (b) the performance of HCHO removal in primordial BAC, 15%Er_{0.5}Mn_{0.5}/BAC, 15%Er/BAC, and 15%Mn/BAC. Reaction conditions: 200 ppm HCHO, 6% O₂, N₂ as balance gas, and T = 100–380 °C.

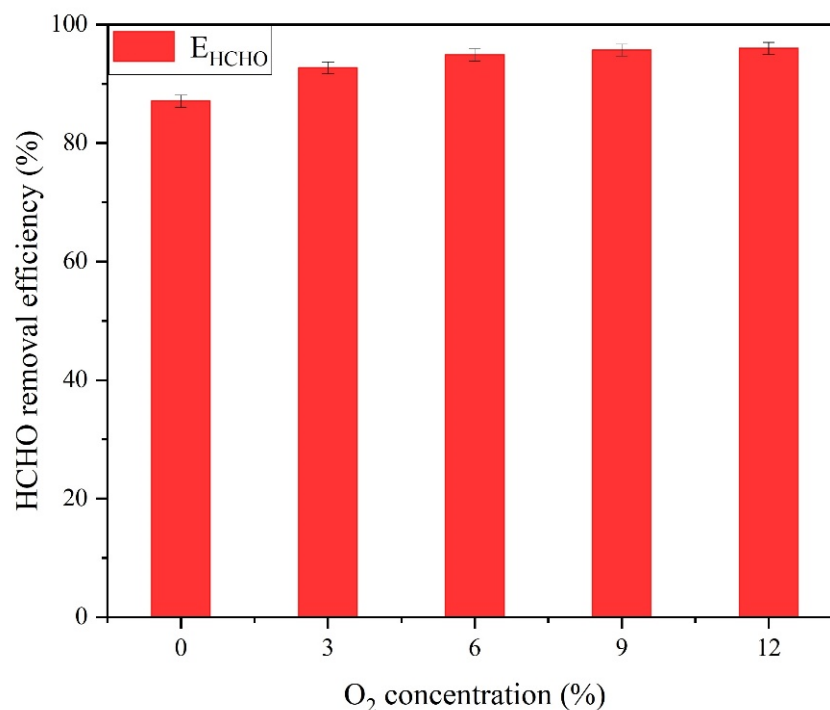


Figure 10. Effect of O₂ on HCHO removal in 15%Er_{0.5}Mn_{0.5}/BAC.

3.3.2. Effects of SO₂ and H₂O

The influences of SO₂ and H₂O on HCHO removal in 15%Er_{0.5}Mn_{0.5}/BAC are shown in Figure 11. In most cases, SO₂ acted as an inhibitor in the removal of HCHO [42]. Compared with the pure SFG, the E_{HCHO} demonstrated a significant downward trend when 300 ppm SO₂ was added, but this trend gently slowed down when the SO₂ increased to 600 and 900 ppm. The former trend can be interpreted in two ways: the first is that SO₂ might compete with HCHO or O₂ for limited adsorption/catalytic active sites, and the second is that SO₂ could readily react with metal oxides in the sample to form metal sulfates, which might cover the surface active sites or block the pores, as demonstrated by in situ DRIFTS [70,71]. The latter trend may be because the introduction of ErO_x or MnO_x could undermine the adsorption intensity of SO₂ on the sample surface, offsetting the inhibitory effect of SO₂ [31]. Likewise, H₂O (g) also had a slight inhibitory effect on the E_{HCHO}. Increasing H₂O by 8% in the SFG reduced the E_{HCHO} from 92.4% to 90.8%, indicating that 15%Er_{0.5}Mn_{0.5}/BAC possessed excellent H₂O resistance resulting from the strong interaction between ErO_x and MnO_x and the hydrophobicity of BAC [72]. Equally, the inhibitory effect of H₂O might be due to the competitive adsorption of the active sites between HCHO and H₂O [73]. The combined additions of SO₂ and H₂O exerted a greater passive effect on the E_{HCHO} than the single addition of SO₂ or H₂O. Nevertheless, under the action of SFG + 600 ppmSO₂ + 8%H₂O, the E_{HCHO} of 15%Er_{0.5}Mn_{0.5}/BAC only decreased by 4.5% from 92.4% to 87.9%, elucidating its excellent anti-SO₂/H₂O performance, which was possibly a result of the positive effect of gaseous H₂O on HCHO potentially related to the active catalytic sites of HCHO [32]. Therefore, it was predicted that 15%Er_{0.5}Mn_{0.5}/BAC displayed exceptional SO₂ and H₂O resistance in the practical flue gas component.

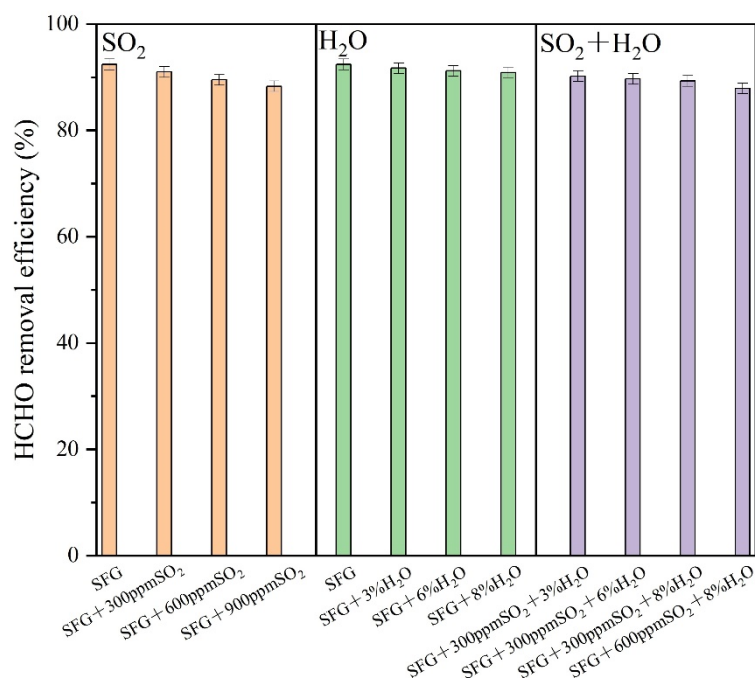


Figure 11. Effects of SO₂ and H₂O on HCHO removal in 15%Er_{0.5}Mn_{0.5}/BAC.

The test results of the stability and selectivity of the 15%Er_{0.5}Mn_{0.5}/BAC catalyst for HCHO removal are presented in Figure 12. Under SFG conditions, the stability test of 15%Er_{0.5}Mn_{0.5}/BAC persisted for 30 h, while the E_{HCHO} decreased from 96.6% to 93.9% in the first 6 h and then remained at approximately 93%. Adding 8%H₂O or 300 ppm SO₂ to the SFG also degraded the E_{HCHO} to almost an identical extent, and their combination amplified this negative trend, which was consistent with the previous performance test analyses. The S_C also exhibited an identical trend, albeit slightly stronger than that of the E_{HCHO}, but the addition of both 8% H₂O and 300 ppm SO₂ impeded their conversion. Some

intermediates, such as DOM and formate, were produced during the removal of HCHO, which was coherent with the results of the subsequent in situ DRIFTS. Eventually, under SFG + 8% H_2O and 300 ppm SO_2 , the E_{HCHO} and S_{C} of 15% $\text{Er}_{0.5}\text{Mn}_{0.5}/\text{BAC}$ were maintained at approximately 85% and 90%, demonstrating distinguished stability and selectivity.

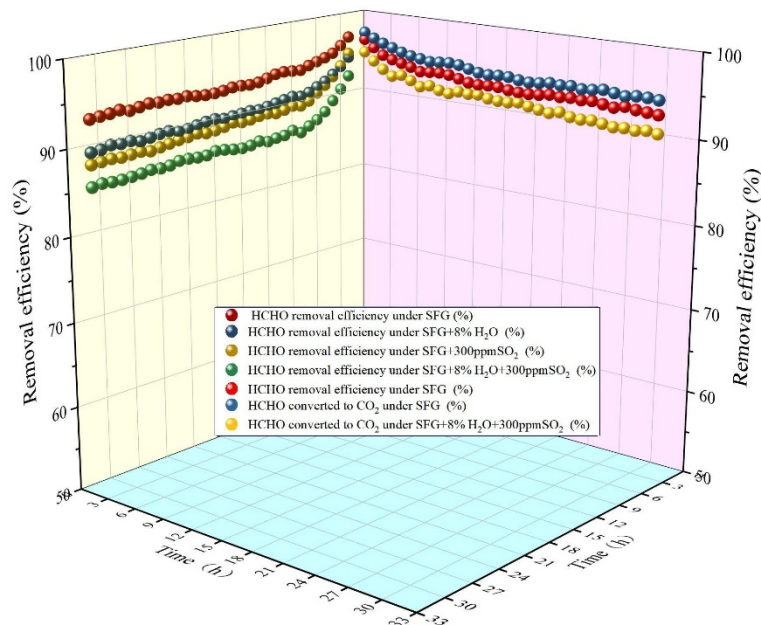


Figure 12. Stability test of HCHO conversion in 15% $\text{Er}_{0.5}\text{Mn}_{0.5}/\text{BAC}$. (Reaction conditions: 200 ppm HCHO, 6% O_2 , N_2 as balance gas, and reaction temperature of 220 °C).

3.4. Intermediates and Mechanism

As reflected in Figure 13, the HCHO reaction processes in the $\text{Er}_{0.5}\text{Mn}_{0.5}/\text{BAC}$ catalyst at 90 min under different test conditions were studied using in situ DRIFTS spectra. The peak associated with molecularly adsorbed HCHO occurred at 1142 cm^{-1} within 10 min after introducing 200 ppm HCHO + 6% O_2/N_2 [74]. In addition, the peak's intensity increased with the reaction time before decreasing slightly after 30 min. The $\omega(\text{CH}_2)$, $\nu(\text{CH}_2)$, and $\nu(\text{C-O})$ of dioxymethylenes were reflected in bands located at 1061, 1014, and 809 cm^{-1} , respectively [74,75]. Following previous studies, it was documented that HCHO was first adsorbed on the sample surface by molecules and then fleetly oxidized into DOM by carbonyl electrophilic carbon combined with nucleophilic surface oxygen [76]. After 10 min, DOM bands were detected and increased with time, showing that the catalytic oxidation reaction of HCHO was still occurring. The paraformaldehyde (POM) produced by the adsorption corresponding to the peak value of 937 cm^{-1} was also rapidly accumulating and continuously generating DOM [75,76]. The amount of DOM reached a stable value as the production of DOM, and its further conversion attained a dynamic equilibrium at 40 min. Moreover, the slight adsorption bands at 1460 and 1385 cm^{-1} could be attributed to the $\nu_{\text{as}}(\text{COO}^-)$ and $\nu_{\text{s}}(\text{COO}^-)$ of formate species, while the $\nu_{\text{as}}(\text{CH})$ and $\nu_{\text{s}}(\text{CH})$ of formate species appeared at 2943 and 2825 cm^{-1} [77,78]. Previous studies have suggested that formates are often adsorbed on the surfaces of catalysts in three frameworks: monodentate, bridging, and bidentate (chelating), which are distinguishable by the frequency of spacings between $\nu_{\text{s}}(\text{COO}^-)$ and $\nu_{\text{as}}(\text{COO}^-)$ [32]. The reduced intensity of the bands in the formate species indicated that the depletion of the formate species was expedited, and DOM oxidation was inhibited until equilibrium was reached after 40 min of the reaction proceeding. The peaks at 1656 cm^{-1} and $2334\text{--}2363\text{ cm}^{-1}$ were related to the formate species' oxidation reactions and conversion to H_2O and CO_2 [41,77,79]. After 10 min of reaction, it was observed that the absorption of CO_2 reached the maximum value before fluctuating and decreasing. The former might have been caused by the rapid catalytic oxidation reaction of HCHO, while the latter was ascribed to the formation of POM blocking the adsorbed active

sites, leading to the desorption of CO_2 in the catalyst [76]. The negative bands at 3484 cm^{-1} and 3690 cm^{-1} were generated by the depletion of hydroxyl ($-\text{OH}$) on the surface, and the adsorption of activated H_2O molecules was continuously replenished by reactive oxygen species [79,80]. The peak at 685 cm^{-1} was attributed to the formation of metallic oxygen bands between Mn or Er ions and carboxyl (COO^-), indicating that ErO_x and MnO_x could serve as active sites during the removal of HCHO [37].

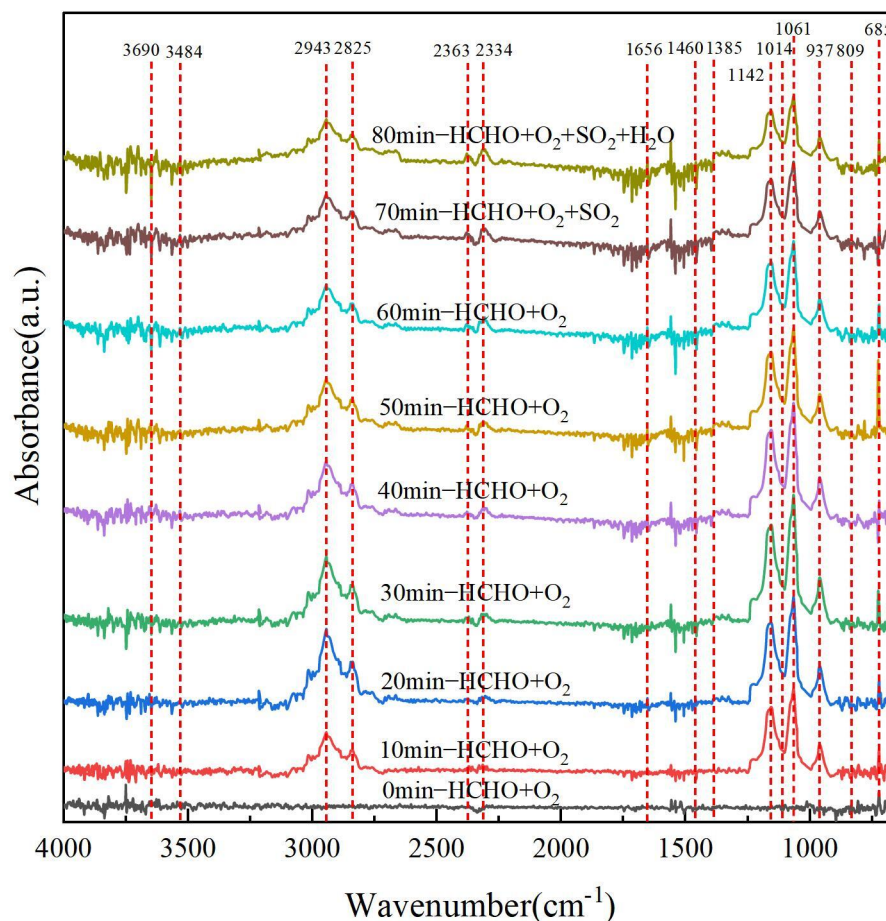


Figure 13. Dynamic changes of in situ DRIFTS for 15% $\text{Er}_{0.5}\text{Mn}_{0.5}/\text{BAC}$ sample as a function of reaction time in a flow of 200 ppm HCHO + 6% O_2/N_2 at $220\text{ }^\circ\text{C}$.

The feasible reaction mechanisms of HCHO removal in 15% $\text{Er}_{0.5}\text{Mn}_{0.5}/\text{BAC}$ were speculated following the characterization analyses and experimental results shown above. It was confirmed that the mechanism of the catalytic oxidation of HCHO by carbon materials supported with metal oxide catalysts followed the Mars–van Krevelen (MVK) mechanism [60]. In this study, catalytic oxidation gradually predominated over adsorption for HCHO removal with the increment in the reaction temperature and time, and the oxidation of HCHO was mainly attributed to the surface reactive oxygen species, including chemisorbed oxygen and lattice oxygen and free radicals on the surfaces of the catalysts, which were expressed as O_γ and OH, respectively. As reflected in Figure 14, HCHO was instantaneously captured by hydroxyl groups and other active sites on the surface of 15% $\text{Er}_{0.5}\text{Mn}_{0.5}/\text{BAC}$. In addition, combined with the results of DRIFTS and other characterization analyses, it was determined that the main gaseous products came from carbonate species and formate intermediates in the HCHO removal process. The latter's production was ascribed to the reaction of surface reactive oxygen species and HCHO to generate DOM, which, in turn, was rapidly oxidized to form formate species. The former's production can be explained by the loss of hydrogen bonds in the formic acid intermediate, further oxidized by the active hydroxyl group to unstable H_2CO_3 , before being converted to CO_2 and H_2O

(Equations (6)–(11)). The subsequent adsorption of HCHO or O₂ was favorable toward H₂O desorption, thus starting a new cycle of HCHO oxidation [81,82]. Throughout the reaction processes, gaseous O₂ and H₂O continuously replenished depleted reactive oxygen species while the redox cycle of Er³⁺/Er²⁺ and Mn⁴⁺/Mn³⁺/Mn²⁺ constantly produced O_γ [25,38]. The introduction of Er species increased the catalytic activity and changed the morphological structures of the catalysts, which was suitable for the TEM and H₂-TPR results. In particular, the hierarchical porous structure of the BAC carrier with suitable ratios of micropores, mesopores, and macropores boosted the reaction paths, which not only furnished abundant surface functional groups but also facilitated the diffusion and mass transfer of reactants and products, thus improving the catalytic oxidation ability of HCHO. In summary, the specific pathways of removing HCHO by 15%Er_{0.5}Mn_{0.5}/BAC can be determined as follows.

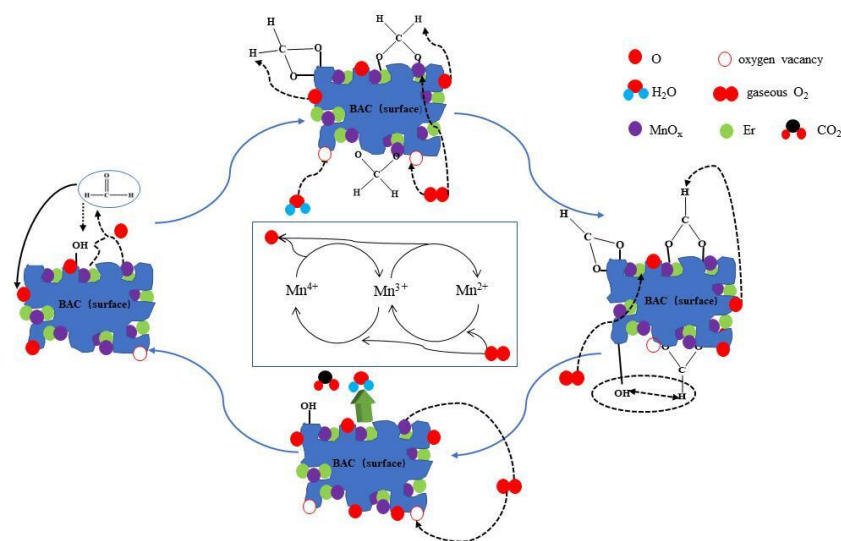
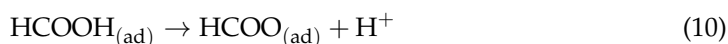
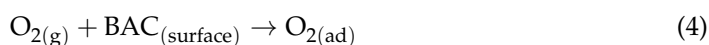
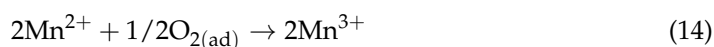
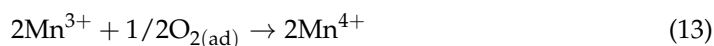


Figure 14. The proposed mechanism of HCHO removal in 15%ErMn/BACs.





4. Computational Details

4.1. DFT Calculation Method

To further clarify the mechanism and reaction process of the catalytic oxidation of HCHO in 15%Er_{0.5}Mn_{0.5}/BAC, current first principle DFT calculations were carried out using the Vienna Ab initio Simulation Package (VASP) with the projector augmented wave (PAW) method [83]. The commutative functional was treated employing the generalized gradient approximation (GGA) of the Perdew–Burke–Ernzerhof (PBE) functional. All calculations were conducted with spin polarizations. The energy cut-off value of the plane wave base expansion was set to 450 eV, and the force on each atom was less than 0.03 eV/Å, which was utilized as the convergence criterion of geometric relaxation. A 2 × 2 × 1 grid was used to sample k points in the Brillouin region. A convergence energy threshold of 10^{−5} eV was adopted in the self-consistent calculations. The DFT-D3 method was utilized to take into account the van der Waals interaction [84]. A 15 Å vacuum was joined in the z direction to prevent the interaction from periodic structures.

The free energies were calculated using the following formula: $\Delta G = \Delta E_{\text{DFT}} + \Delta E_{\text{ZPE}} - T\Delta S$, where ΔE_{DFT} is the DFT electronic energy difference at each step, ΔE_{ZPE} and ΔS are the correction of zero-point energy and the change in entropy, respectively, acquired via vibration analysis, and T is the temperature (T = 300 K) [85].

4.2. HCHO Oxidation Reaction Path Diagram of MnO₂ and Er-MnO₂

To prove that Er doping contributed to the HCHO catalytic oxidation reaction and its mechanism, Figure 15 shows the reaction path and configuration of MnO_{2−x} (1 1 1) and Er-MnO_{2−x} (1 1 3) in the catalytic oxidation of HCHO, in which the structure and shape of each intermediate for the HCHO conversion to CO₂ and H₂O are observed. In addition, the formaldehyde oxidation reaction paths of the Er-MnO₂ and MnO₂ structures were calculated, as shown in Figure 16. It can be seen that the MnO₂ structure was stronger than the Er-MnO₂ structure in the first step of formaldehyde adsorption activation, with an adsorption-free energy of −2.08 eV, while that of the Er-MnO₂ structure was only −0.53 eV. After a series of calculations, it was found that the rate determination step of the MnO₂ structure reaction was a CH₂O₂* → CO₂* transfer step, and the rate determination step energy barrier was 0.95 eV, while the decisive step of the Er-MnO₂ structure reaction was an HCOO* → CO₂* step, and the energy barrier of the decisive step was 0.80 eV. The reduction in the energy barrier of the decisive step indicates that the Er-MnO₂ structure promoted the formaldehyde oxidation process. This result is consistent with the in situ DRIFTS, and the incorporation of Er promoted the catalytic oxidation of HCHO to a certain extent.

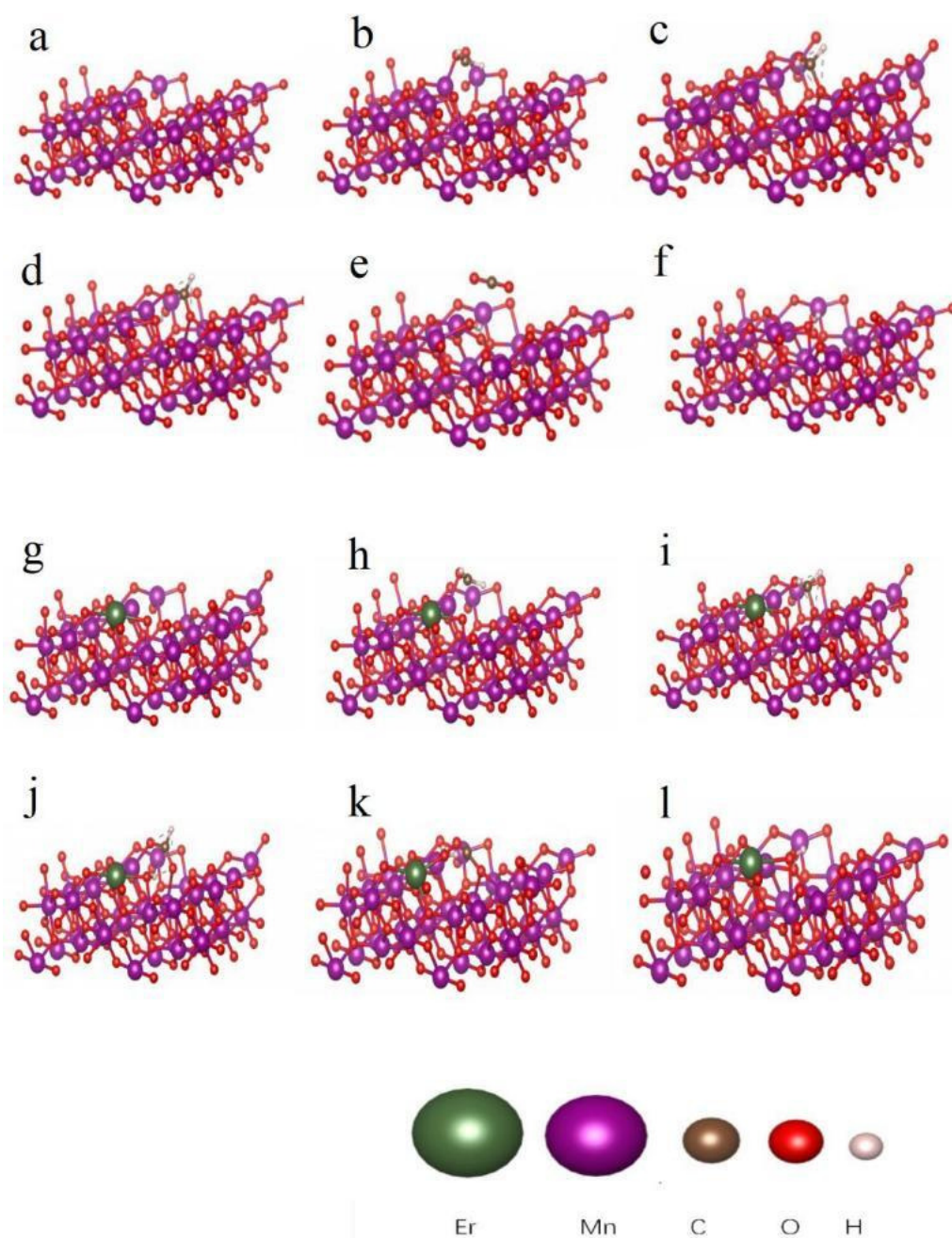


Figure 15. The reaction configurations of MnO_{2-x} (1 1 1) and Er-MnO_{2-x} (1 1 3) catalyzed oxidation of HCHO: (a) MnO_{2-x} , (b) $\text{MnO}_{2-x}\text{-CH}_2\text{O}^*$, (c) $\text{MnO}_{2-x}\text{-CH}_2\text{O}_2^*$, (d) $\text{MnO}_{2-x}\text{-HCOO}^*$, (e) $\text{MnO}_{2-x}\text{-CO}_2^*$, (f) $\text{MnO}_{2-x}\text{-H}_2\text{O}^*$, (g) Er-MnO_{2-x} , (h) $\text{Er-MnO}_{2-x}\text{-CH}_2\text{O}^*$, (i) $\text{Er-MnO}_{2-x}\text{-CH}_2\text{O}_2^*$, (j) $\text{Er-MnO}_{2-x}\text{-HCOO}^*$, (k) $\text{Er-MnO}_{2-x}\text{-CO}_2^*$, and (l) $\text{Er-MnO}_{2-x}\text{-H}_2\text{O}^*$.

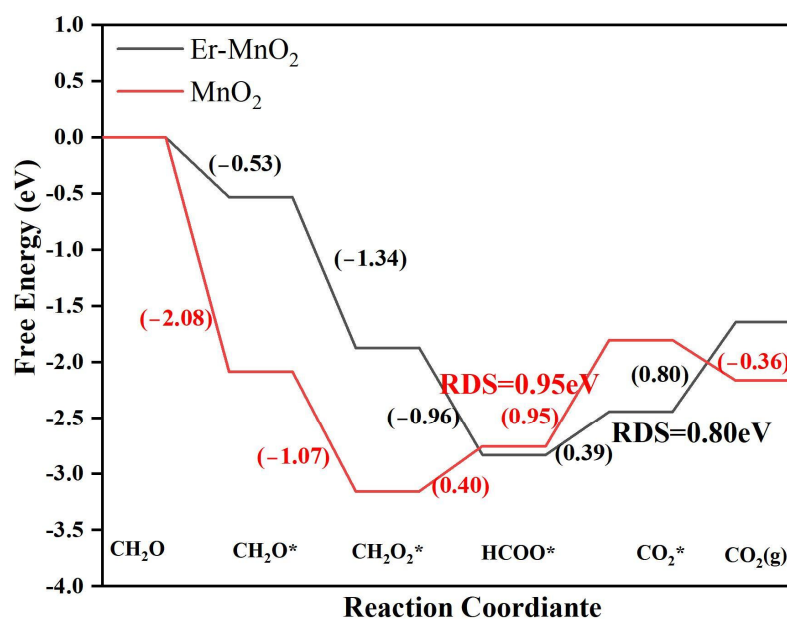


Figure 16. Calculation of reaction path free energy for catalytic oxidation of HCHO.

5. Conclusions

A series of ErO_x-boosted MnO_x-modified biochars derived from rice straw and sewage sludge (Er_yMn_{1-y}/BACs) were prepared using the facile ultrasonic-assisted impregnation method, and their HCHO removal activities were subsequently tested. The optimal 15%Er_{0.5}Mn_{0.5}/BAC displayed a 97.2% HCHO removal efficiency at 220 °C and excellent stability throughout the circulation experiment. The removal mechanism of HCHO in 15%Er_{0.5}Mn_{0.5}/BAC was systematically studied using BET, H₂-TPR, SEM, TEM, XRD, in situ DRIFTS, XPS, and density-functional theory (DFT). The effects of O₂, SO₂, and H₂O on HCHO removal in 15%Er_{0.5}Mn_{0.5}/BAC were tested, and the curbed influences of H₂O and SO₂ offset the boosting effect of O₂ within a certain range. Er–Mn bimetallic-modified BAC offered a superior HCHO removal performance than that of Er- or Mn-boosted BAC, owing to the synergistic effect of ErO_x and MnO_x conducive to improving the samples' total pore volumes and surface areas, the surface active oxygen species, the promotion of redox ability, and the inhibition of the crystallization of MnO_x. Moreover, the support's hierarchical porous structure not only expedited the diffusion and mass transfer of reactants and their products but also elevated the approachability of adsorption and catalytic sites. Notably, these prominent features were partly responsible for the outstanding performance and excellent tolerance to H₂O and SO₂. In situ DRIFTS showed the appearance of CO₂ and H₂O during the oxidation of HCHO to DOM and formate intermediates. The DFT calculations proved the removal process of HCHO and the strengthening effect of Er doping. Finally, this work provides direction and guidance for the future development of outstanding biochars-based catalysts for HCHO removal.

Author Contributions: Validation, resources, data curation, and writing—original draft preparation, J.W. (Jiajie Wang); conceptualization, methodology, validation, project administration, and funding acquisition, L.G.; visualization and writing—review and editing, D.X.; methodology, writing—review and editing, and funding acquisition, C.L.; visualization, L.X.; formal analysis, Y.J.; data curation, Q.X.; investigation, H.X.; formal analysis, L.Y.; writing—original draft preparation, J.L.; writing—original draft preparation, J.W. (Jiajun Wu). All authors have read and agreed to the published version of the manuscript.

Funding: This study was financially supported by the Scientific Research Project of the Hunan Provincial Department of Education (22B0458) and the National Natural Science Foundation of China (52270102).

Data Availability Statement: The data are contained within this article.

Acknowledgments: The authors thank the University of South China and Hunan University for their experimental situational support.

Conflicts of Interest: The authors declare no conflict of interest.

References

1. Yang, C.; Miao, G.; Pi, Y.; Xia, Q.; Wu, J.; Li, Z.; Xiao, J. Abatement of various types of VOCs by adsorption/catalytic oxidation: A review. *Chem. Eng. J.* **2019**, *370*, 1128–1153. [[CrossRef](#)]
2. Li, X.; Zhang, L.; Yang, Z.; Wang, P.; Yan, Y.; Ran, J. Adsorption materials for volatile organic compounds (VOCs) and the key factors for VOCs adsorption process: A review. *Sep. Purif.* **2020**, *235*, 116213. [[CrossRef](#)]
3. Zhao, L.; Li, C.; Du, X.; Zeng, G.; Gao, L.; Zhai, Y.; Wang, T.; Zhang, J. Effect of Co addition on the performance and structure of V/ZrCe catalyst for simultaneous removal of NO and Hg⁰ in simulated flue gas. *Appl. Surf. Sci.* **2018**, *437*, 390–399. [[CrossRef](#)]
4. He, C.; Cheng, J.; Zhang, X.; Douthwaite, M.; Pattison, S.; Hao, Z.P. Recent advances in the catalytic oxidation of volatile organic compounds: A review based on pollutant sorts and sources. *Chem. Rev.* **2019**, *119*, 4471–4568. [[CrossRef](#)]
5. Zhang, X.; Zhao, W.; Nie, L.; Shao, X.; Dang, H.; Zhang, W.; Wang, D. A new classification approach to enhance future VOCs emission policies: Taking solvent-consuming industry as an example. *Environ. Pollut.* **2021**, *268*, 115868. [[CrossRef](#)]
6. Ye, J.; Yu, Y.; Fan, J.; Cheng, B.; Yu, J.; Ho, W. Room-temperature formaldehyde catalytic decomposition. *Environ. Sci. Nano.* **2020**, *7*, 3655–3709. [[CrossRef](#)]
7. Chen, D.; Zhang, G.; Wang, M.; Li, N.; Xu, Q.; Li, H.; He, J.; Lu, J. Pt/MnO₂ Nanoflowers Anchored to Boron Nitride Aerogels for Highly Efficient Enrichment and Catalytic Oxidation of Formaldehyde at Room Temperature. *Angew. Chem. Int. Ed.* **2021**, *133*, 6447–6451. [[CrossRef](#)]
8. Xu, Y.; Dhainaut, J.; Dacquin, J.-P.; Mamede, A.-S.; Marinova, M.; Lamonier, J.-F.; Vezin, H.; Zhang, H.; Royer, S. La_{1-x}(Sr, Na, K)_xMnO₃ perovskites for HCHO oxidation: The role of oxygen species on the catalytic mechanism. *Appl. Catal. B Environ.* **2021**, *287*, 119955. [[CrossRef](#)]
9. Ding, J.; Liu, J.; Yang, Y.; Zhao, L.; Yu, Y. Understanding A-site tuning effect on formaldehyde catalytic oxidation over La-Mn perovskite catalysts. *J. Hazard. Mater.* **2022**, *422*, 126931. [[CrossRef](#)]
10. Zhou, C.; Zhang, H.; Zhang, Z.; Li, L. Improved reactivity for toluene oxidation on MnO_x/CeO₂-ZrO₂ catalyst by the synthesis of cubic-tetragonal interfaces. *Appl. Surf. Sci.* **2021**, *539*, 148188. [[CrossRef](#)]
11. Hen, Y.; Liao, Y.; Chen, L.; Chen, S.; Chen, Z.; Ma, X. Heavy metals impregnated TiO₂ catalysts for the multi-pollution reduction of coal-fired flue gas. *J. Environ. Chem. Eng.* **2021**, *9*, 105822.
12. Gao, L.; Yi, L.; Xie, D.; Wang, H.; Li, C.; Li, L.; Liu, Y.; Xie, J.; Zhou, Y.; Liu, Y. Insight into the design and construction of Cr substituted Co-based columnar activated coke catalysts for effective and reliable removal of methylbenzene and Hg⁰ concurrently. *Fuel* **2023**, *334*, 126732. [[CrossRef](#)]
13. Cai, T.; Deng, W.; Xu, P.; Yuan, J.; Liu, Z.; Zhao, K.; Tang, Q.; He, D. Great activity enhancement of Co₃O₄/γ-Al₂O₃ catalyst for propane combustion by structural modulation. *Chem. Eng. J.* **2020**, *395*, 125071. [[CrossRef](#)]
14. Wang, A.-Y.; Sun, K.; Wu, L.; Wu, P.; Zeng, W.; Tian, Z.; Huang, Q.-X. Co-carbonization of biomass and oily sludge to prepare sulfamethoxazole super-adsorbent materials. *Sci. Total Environ.* **2020**, *698*, 134238. [[CrossRef](#)]
15. Qie, Z.; Sun, F.; Zhang, Z.; Pi, X.; Qu, Z.; Gao, J.; Zhao, G. A facile trace potassium assisted catalytic activation strategy regulating pore topology of activated coke for combined removal of toluene/SO₂/NO. *Chem. Eng. J.* **2020**, *389*, 124262. [[CrossRef](#)]
16. Xiao, G.; Guo, Z.; Li, J.; Du, Y.; Zhang, Y.; Xiong, T.; Lin, B.; Fu, M.; Ye, D.; Hu, Y. Insights into the effect of flue gas on synergistic elimination of toluene and NO_x over V₂O₅-MoO₃(WO₃)/TiO₂ catalysts. *Chem. Eng. J.* **2022**, *435*, 134914. [[CrossRef](#)]
17. Liu, K.; Wang, S.; Wu, Q.; Wang, L.; Ma, Q.; Zhang, L.; Li, G.; Tian, H.; Duan, L.; Hao, J. A highly resolved mercury emission inventory of chinese coal-fired power plants. *Environ. Sci. Technol.* **2018**, *52*, 2400–2408. [[CrossRef](#)] [[PubMed](#)]
18. Wang, Y.; Jiang, C.; Le, Y.; Cheng, B.; Yu, J. Hierarchical honeycomb-like Pt/NiFe-LDH/rGO nanocomposite with excellent formaldehyde decomposition activity. *Chem. Eng. J.* **2019**, *365*, 378–388. [[CrossRef](#)]
19. Yusuf, A.; Sun, Y.; Liu, S.; Wang, C.; Ren, Y.; Xiao, H.; Snape, C.; He, J. Study of the effect of ceria on the activity and selectivity of Co and Ce co-doped birnessite manganese oxide for formaldehyde oxidation. *J. Hazard. Mater.* **2022**, *424*, 127583. [[CrossRef](#)]
20. Wang, J.; Yoshida, A.; Wang, P.; Yu, T.; Wang, Z.; Hao, X.; Abudula, A.; Guan, G. Catalytic oxidation of volatile organic compound over cerium modified cobalt-based mixed oxide catalysts synthesized by electrodeposition method. *Appl. Catal. B Environ.* **2020**, *271*, 118941. [[CrossRef](#)]
21. Ma, C.; Yang, C.; Wang, B.; Chen, C.; Wang, F.; Yao, X.; Song, M. Effects of H₂O on HCHO and CO oxidation at room-temperature catalyzed by MCo₂O₄. *Appl. Catal. B Environ.* **2019**, *254*, 76–85. [[CrossRef](#)]
22. Todorova, S.; Blin, J.L.; Naydenov, A.; Lebeau, B.; Kolev, H.; Gaudin, P.; Dotezva, A.; Velinova, R.; Filkova, D.; Ivanova, I.; et al. Co₃O₄-MnO_x oxides supported on SBA-15 for CO and VOCs oxidation. *Catal. Today* **2020**, *357*, 602–612. [[CrossRef](#)]
23. Kim, S.C.; Shim, W.G. Catalytic combustion of VOCs over a series of manganese oxide catalysts. *Appl. Catal. B Environ.* **2010**, *98*, 180–185. [[CrossRef](#)]

24. Liang, X.; Liu, P.; He, H.; Wei, G.; Chen, T.; Tan, W.; Tan, F.; Zhu, J.; Zhu, R. The variation of cationic microstructure in Mn-doped spinel ferrite during calcination and its effect on formaldehyde catalytic oxidation. *J. Hazard. Mater.* **2016**, *306*, 305–312. [[CrossRef](#)] [[PubMed](#)]
25. Gao, L.; Li, C.; Li, S.; Zhang, W.; Du, X.; Huang, L.; Zhu, Y.; Zhai, Y.; Zeng, G. Superior performance and resistance to SO₂ and H₂O over CoO_x-modified MnO_x/biomass activated carbons for simultaneous Hg⁰ and NO removal. *Chem. Eng. J.* **2019**, *371*, 781–795. [[CrossRef](#)]
26. Du, H.; Han, Z.; Wu, X.; Li, C.; Gao, Y.; Yang, S.; Song, L.; Dong, J.; Pan, X. Insight into the Promoting Role of Er Modification on SO₂ Resistance for NH₃-SCR at Low Temperature over FeMn/TiO₂ Catalysts. *Catalysts* **2021**, *11*, 618. [[CrossRef](#)]
27. Jin, Q.; Shen, Y.; Zhu, S.; Li, X.; Hu, M. Promotional effects of Er incorporation in CeO₂(ZrO₂)/TiO₂ for selective catalytic reduction of NO by NH₃. *Chin. J. Catal.* **2016**, *37*, 1512–1528. [[CrossRef](#)]
28. Kim, J.; Lee, S.; Kwon, D.W.; Ha, H.P. Er composition (X)-mediated catalytic properties of Ce_{1-x}Er_xVO₄ surfaces for selective catalytic NO_x reduction with NH₃ at elevated temperatures. *Catal. Today* **2021**, *359*, 65–75. [[CrossRef](#)]
29. Gao, L.; Li, C.; Zhang, J.; Du, X.; Li, S.; Zeng, J.; Yi, Y.; Zeng, G. Simultaneous removal of NO and Hg⁰ from simulated flue gas over CoO_x-CeO₂ loaded biomass activated carbon derived from maize straw at low temperatures. *Chem. Eng. J.* **2018**, *342*, 339–349. [[CrossRef](#)]
30. Zhang, G.; Xing, J.; Zhao, Y.; Yang, F. Hierarchical N,P co-doped graphene aerogels framework assembling vertically grown CoMn-LDH nanosheets as efficient bifunctional electrocatalyst for rechargeable Zinc-air battery. *J. Colloid Interface Sci.* **2021**, *590*, 476–486. [[CrossRef](#)]
31. Gao, L.; Yi, L.; Wang, J.; Li, X.; Feng, Z.; Shan, J.; Liu, Y.; Tan, W.; He, Q.; Li, C. Excellent performance and outstanding resistance to SO₂ and H₂O for formaldehyde abatement over CoMn oxides boosted dual-precursor hierarchical porous biochars derived from liquidambar and orange peel. *Fuel* **2022**, *317*, 123539. [[CrossRef](#)]
32. Du, X.; Li, C.; Zhang, J.; Zhao, L.; Li, S.; Lyu, Y.; Zhang, Y.; Zhu, Y.; Huang, L. Highly efficient simultaneous removal of HCHO and elemental mercury over Mn-Co oxides promoted Zr-AC samples. *J. Hazard. Mater.* **2021**, *408*, 124830. [[CrossRef](#)] [[PubMed](#)]
33. Cui, W.; Li, Y.; Zhang, H.; Wei, Z.; Gao, B.; Dai, J.; Hu, T. In situ encapsulated Co/MnO_x nanoparticles inside quasi-MOF-74 for the higher alcohols synthesis from syngas. *Appl. Catal. B Environ.* **2020**, *278*, 119262. [[CrossRef](#)]
34. Gao, L.; Li, C.; Lu, P.; Zhang, J.; Du, X.; Li, S.; Tang, L.; Chen, J.; Zeng, G. Simultaneous removal of Hg⁰ and NO from simulated flue gas over columnar activated coke granules loaded with La₂O₃-CeO₂ at low temperature. *Fuel* **2018**, *215*, 30–39. [[CrossRef](#)]
35. Xia, C.; Zhou, Y.; He, C.; Douka, A.I.; Guo, W.; Qi, K.; Xia, B. Recent advances on electrospun nanomaterials for zinc–air batteries. *Small Sci.* **2021**, *1*, 2100010. [[CrossRef](#)]
36. Yi, L.; Xie, J.; Li, C.; Shan, J.; Liu, Y.; Lv, J.; Li, M.; Gao, L. LaOx modified MnO_x loaded biomass activated carbon and its enhanced performance for simultaneous abatement of NO and Hg⁰. *Environ. Sci. Pollut. Res.* **2022**, *29*, 2258–2275. [[CrossRef](#)]
37. Du, X.; Li, C.; Zhao, L.; Zhang, J.; Gao, L.; Sheng, J.; Yi, Y.; Chen, J.; Zeng, G. Promotional removal of HCHO from simulated flue gas over Mn-Fe oxides modified activated coke. *Appl. Catal. B Environ.* **2018**, *232*, 37–48. [[CrossRef](#)]
38. Rajesh, M.; Babu, M.R.; Sushma, N.J.; Raju, B.D.P. Influence of Er³⁺ ions on structural and fluorescence properties of SiO₂-B₂O₃-Na₂CO₃-NaF-CaF₂ glasses for broadband 1.53 μm optical amplifier applications. *J. Non-Cryst. Solids* **2019**, *599*, 119732. [[CrossRef](#)]
39. Wang, Z.; Chen, B.; Crocker, M.; Yu, L.; Shi, C. New insights into alkaline metal modified CoMn-oxide catalysts for formaldehyde oxidation at low temperatures. *Appl. Catal. A Gen.* **2020**, *596*, 117512. [[CrossRef](#)]
40. Ding, J.; Liu, J.; Yang, Y.; Wang, Z.; Yu, Y. Reaction mechanism of dichloromethane oxidation on LaMnO₃ perovskite. *J. Hazard. Mater.* **2021**, *277*, 130194. [[CrossRef](#)]
41. Li, R.; Huang, Y.; Zhu, D.; Ho, W.; Cao, J.; Lee, S. Improved oxygen activation over a Carbon/Co₃O₄ nanocomposite for efficient catalytic oxidation of formaldehyde at room temperature. *Environ. Sci. Technol.* **2021**, *55*, 4054–4063. [[CrossRef](#)] [[PubMed](#)]
42. Zhao, T.; Qiu, P.; Fan, Y.; Yang, J.; Jiang, W.; Wang, L.; Deng, Y.; Luo, W. Hierarchical branched mesoporous TiO₂-SnO₂ nanocomposites with well-defined n-n heterojunctions for highly efficient ethanol sensing. *Adv. Sci.* **2019**, *6*, 1902008. [[CrossRef](#)] [[PubMed](#)]
43. Boningari, T.; Ettireddy, P.; Somogyvari, A.; Liu, Y.; Vorontsov, A.; McDonald, C.; Smirniotis, P. Influence of elevated surface texture hydrated titania on Ce-doped Mn/TiO₂ catalysts for the low-temperature SCR of NO_x under oxygen-rich conditions. *J. Catal.* **2015**, *325*, 145–155. [[CrossRef](#)]
44. Jiang, L.; Liu, Q.; Ran, G.; Kong, M.; Ren, S.; Yang, J.; Li, J. V₂O₅-modified Mn-Ce/AC catalyst with high SO₂ tolerance for low-temperature NH₃-SCR of NO. *Chem. Eng. J.* **2019**, *370*, 810–821. [[CrossRef](#)]
45. Castano, M.H.; Molina, R.; Moreno, S. Cooperative effect of the Co–Mn mixed oxides for the catalytic oxidation of VOCs: Influence of the synthesis method. *Appl. Catal. A Gen.* **2015**, *492*, 48–59. [[CrossRef](#)]
46. Fan, Y.; Sun, M.; Miao, C.; Yue, Y.; Hua, W.; Gao, Z. Morphology Effects of Nanoscale Er₂O₃ and Sr-Er₂O₃ Catalysts for Oxidative Coupling of Methane. *Catal. Lett.* **2021**, *151*, 2197–2206. [[CrossRef](#)]
47. Chen, Y.; Zheng, D.; Li, L.; Zeng, M.; Qin, M.; Hou, Z.; Fan, Z.; Gao, X.; Lu, X.; Li, Q.; et al. Domain structure and multiferroic properties of epitaxial hexagonal ErMnO₃ films. *J. Alloys Compd.* **2020**, *821*, 153529. [[CrossRef](#)]
48. Van, T.T.; Hoang, J.; Ostroumov, R.; Wang, K.L.; Bargar, J.R.; Lu, J.; Blom, H.O.; Chang, J.P. Nanostructure and temperature-dependent photoluminescence of Er-doped Y₂O₃ thin films for micro-optoelectronic integrated circuits. *J. Appl. Phys.* **2006**, *100*, 073512. [[CrossRef](#)]

49. Shen, B.; Liu, Z.; Xu, H.; Wang, F. Enhancing the absorption of elemental mercury using hydrogen peroxide modified bamboo carbons. *Fuel* **2019**, *235*, 878–885. [[CrossRef](#)]
50. Huang, H.; Hu, P.; Huang, H.; Chen, J.; Ye, X.; Leung, D.Y.C. Highly dispersed and active supported Pt nanoparticles for gaseous formaldehyde oxidation: Influence of particle size. *Chem. Eng. J.* **2014**, *252*, 320–326. [[CrossRef](#)]
51. Wu, H.; Li, C.; Zhao, L.; Zhang, J.; Zeng, G.; Xie, Y.; Zhang, X.; Wang, Y. Removal of gaseous elemental mercury by cylindrical activated coke loaded with $\text{CoO}_x\text{-CeO}_2$ from simulated coal combustion flue gas. *Energy Fuels* **2015**, *29*, 6747–6757. [[CrossRef](#)]
52. Zhang, H.; Li, S.; Jiao, Y.; Iojoiu, E.E.; Costa, P.D.; Galvez, M.E.; Chen, Y. Structure, surface and reactivity of activated carbon: From model soot to Bio Diesel soot. *Fuel* **2019**, *257*, 116038. [[CrossRef](#)]
53. Li, Y.; Liu, Y.; Yang, W.; Liu, L.; Pan, J. Adsorption of elemental mercury in flue gas using biomass porous carbons modified by microwave/hydrogen peroxide. *Fuel* **2021**, *291*, 120152. [[CrossRef](#)]
54. Wu, X.; Yu, X.; Huang, Z.; Shen, H.; Jing, G. MnO_x -decorated VO_x/CeO_2 catalysts with preferentially exposed {110} facets for selective catalytic reduction of NO_x by NH_3 . *Appl. Catal. B Environ.* **2020**, *268*, 118419. [[CrossRef](#)]
55. He, J.; Yao, P.; Qiu, J.; Zhang, H.; Jiao, Y.; Wang, J.; Chen, Y. Enhancement effect of oxygen mobility over $\text{Ce}_{0.5}\text{Zr}_{0.5}\text{O}_2$ catalysts doped by multivalent metal oxides for soot combustion. *Fuel* **2021**, *286*, 119359. [[CrossRef](#)]
56. Li, G.; Wang, B.; Zhang, J.; Wang, R.; Liu, H. Er-doped g- C_3N_4 for photodegradation of tetracycline and tylosin: High photocatalytic activity and low leaching toxicity. *Chem. Eng. J.* **2019**, *453*, 123500. [[CrossRef](#)]
57. Gul, S.; Serna, M.; Zahra, S.; Arif, N.; Iqbal, M.; Akinwande, D.; Rizwan, S. Un-doped and Er-adsorbed layered Nb_2C MXene for efficient hydrazine sensing application. *Surf. Interfaces* **2021**, *24*, 101074. [[CrossRef](#)]
58. Liu, M.; Li, C.; Zeng, Q.; Du, X.; Gao, L.; Li, S.; Zhai, Y. Study on removal of elemental mercury over $\text{MoO}_3\text{-CeO}_2$ /cylindrical activated coke in the presence of SO_2 by Hg-temperature-programmed desorption. *Chem. Eng. J.* **2019**, *371*, 666–678. [[CrossRef](#)]
59. Chen, J.; Li, C.; Li, S.; Lu, P.; Gao, L.; Du, X.; Yi, Y. Simultaneous removal of HCHO and elemental mercury from flue gas over Co-Ce oxides supported activated coke impregnated by sulfuric acid. *Chem. Eng. J.* **2018**, *338*, 358–368. [[CrossRef](#)]
60. Miao, L.; Wang, J.; Zhang, P. Review on manganese dioxide for catalytic oxidation of airborne formaldehyde. *Appl. Surf. Sci.* **2019**, *466*, 441–453. [[CrossRef](#)]
61. Liu, F.; Cao, R.; Rong, S.; Zhang, P. Tungsten doped manganese dioxide for efficient removal of gaseous formaldehyde at ambient temperatures. *Mater. Des.* **2018**, *149*, 165–172. [[CrossRef](#)]
62. Ullah, H.; Abbas, Q.; Ali, M.U.; Amina; Cheema, A.I.; Yousaf, B.; Rinklebe, J. Synergistic effects of low-/medium-vacuum carbonization on physicochemical properties and stability characteristics of biochars. *Chem. Eng. J.* **2019**, *373*, 44–57. [[CrossRef](#)]
63. Lam, S.S.; Liew, R.K.; Wong, Y.M.; Azwar, E.; Jusoh, A.; Wahi, R. Activated carbon for catalyst support from microwave pyrolysis of orange peel. *Waste Biomass Valor.* **2017**, *8*, 2109–2119. [[CrossRef](#)]
64. Zhao, Q.; Chen, B.; Li, J.; Wang, X.; Crocker, M.; Shi, C. Insights into the structure-activity relationships of highly efficient CoMn oxides for the low temperature $\text{NH}_3\text{-SCR}$ of NO_x . *Appl. Catal. B Environ.* **2020**, *277*, 119215. [[CrossRef](#)]
65. Li, H.; Wu, C.-Y.; Li, Y.; Zhang, J. $\text{CeO}_2\text{-TiO}_2$ catalysts for catalytic oxidation of elemental mercury in low-rank coal combustion flue gas. *Environ. Sci. Technol.* **2011**, *45*, 7394–7400. [[CrossRef](#)] [[PubMed](#)]
66. Lu, P.; Li, C.; Zeng, G.; He, L.; Peng, D.; Cui, H.; Li, S.; Zhai, Y. Low temperature selective catalytic reduction of NO by activated carbon fiber loading lanthanum oxide and ceria. *Appl. Catal. B Environ.* **2010**, *96*, 157–161. [[CrossRef](#)]
67. Zhang, S.; Wang, H.; Si, H.; Jia, X.; Wang, Z.; Li, Q.; Kong, J.; Zhang, J. Novel core-shell ($\text{#MnO}_2/\text{CeO}_2$)@ CeO_2 composite catalyst with a synergistic effect for efficient formaldehyde oxidation. *ACS Appl. Mater. Interfaces* **2020**, *12*, 40285.
68. Zhang, Y.; Li, C.; Zhu, Y.; Du, X.; Lyu, Y.; Li, S.; Zhai, Y. Insight into the enhanced performance of toluene removal from simulated flue gas over Mn-Cu oxides modified activated coke. *Fuel* **2020**, *276*, 118099. [[CrossRef](#)]
69. Zhang, J.; Shen, B.; Hu, Z.; Zhen, M.; Guo, S.; Dong, F. Uncovering the synergy between Mn substitution and O vacancy in ZnAl-LDH photocatalyst for efficient toluene removal. *Appl. Catal. B Environ.* **2021**, *296*, 120376. [[CrossRef](#)]
70. Wang, T.; Li, C.; Zhao, L.; Zhang, J.; Li, S.; Zeng, G. The catalytic performance and characterization of ZrO_2 support modification on $\text{CuO-CeO}_2/\text{TiO}_2$ catalyst for the simultaneous removal of Hg^0 and NO. *Appl. Surf. Sci.* **2017**, *400*, 227–237. [[CrossRef](#)]
71. Zhuang, Z.; Wang, L.; Tang, J. Efficient removal of volatile organic compound by ballmilled biochars from different preparing conditions. *J. Hazard. Mater.* **2021**, *406*, 124676. [[CrossRef](#)] [[PubMed](#)]
72. Lyu, Y.; Li, C.; Du, X.; Zhu, Y.; Zhang, Y.; Li, S. Catalytic oxidation of toluene over MnO_2 catalysts with different Mn (II) precursors and the study of reaction pathway. *Fuel* **2020**, *262*, 116610. [[CrossRef](#)]
73. Ma, C.; Sun, S.; Lu, H.; Hao, Z.; Yang, C.; Wang, B.; Chen, C.; Song, M. Remarkable MnO_2 structure-dependent H_2O promoting effect in HCHO oxidation at room temperature. *J. Hazard. Mater.* **2021**, *414*, 125542. [[CrossRef](#)] [[PubMed](#)]
74. Wang, Y.; Qu, Z.; Xu, J.; Huang, B. Effect of Al_2O_3 phase on the catalytic performance for HCHO oxidation over $\text{Ag}/\text{Al}_2\text{O}_3$ catalysts. *Appl. Catal. A Gen.* **2020**, *602*, 117705. [[CrossRef](#)]
75. Bao, W.; Chen, H.; Wang, H.; Zhang, R.; Wei, Y.; Zheng, L. Pt nanoparticles supported on N/Ce-doped activated carbon for the catalytic oxidation of formaldehyde at room temperature. *ACS Appl. Nano Mater.* **2020**, *3*, 2614–2624. [[CrossRef](#)]
76. Xiang, N.; Hou, Y.; Han, X.; Li, Y.; Guo, Y.; Liu, Y.; Huang, Z. Promoting effect and mechanism of alkali Na on Pd/SBA-15 for room temperature formaldehyde catalytic oxidation. *ChemCatChem* **2019**, *11*, 5098–5107. [[CrossRef](#)]
77. Ye, J.; Zhou, M.; Le, Y.; Cheng, B.; Yu, J. Three-dimensional carbon foam supported MnO_2/Pt for rapid capture and catalytic oxidation of formaldehyde at room temperature. *Appl. Catal. B Environ.* **2020**, *267*, 118689. [[CrossRef](#)]

78. Hou, Z.; Dai, L.; Liu, Y.; Deng, J.; Jing, L.; Pei, W.; Gao, R.; Feng, Y.; Dai, H. Highly efficient and enhanced sulfur resistance supported bimetallic single-atom palladium–cobalt catalysts for benzene oxidation. *Appl. Catal. B Environ.* **2021**, *285*, 119844. [[CrossRef](#)]
79. Chen, H.; Zhang, R.; Wang, H.; Bao, W.; Wei, Y. Encapsulating uniform Pd nanoparticles in TS-1 zeolite as efficient catalyst for catalytic abatement of indoor formaldehyde at room temperature. *Appl. Catal. B Environ.* **2020**, *278*, 119311. [[CrossRef](#)]
80. Eom, H.; Hwang, I.-H.; Lee, D.; Lee, S.M.; Kim, S.S. Preparation of liquid-phase reduction method-based Pt/TiO₂ catalyst and reaction characteristics during HCHO room temperature oxidation. *Ind. Eng. Chem. Res.* **2020**, *59*, 15489–15496. [[CrossRef](#)]
81. Guo, H.; Li, M.; Liu, X.; Meng, C.; Linguerrri, R.; Han, Y.; Chambaud, G. Fe Atoms Trapped on Graphene as Potential Efficient Catalysts for Room-temperature Complete Oxidation of Formaldehyde: A First-principles Investigation. *Catal. Sci. Technol.* **2017**, *7*, 2012–2021. [[CrossRef](#)]
82. Zhu, J.; Feng, X.; Liu, X.; Zhang, X.; Wu, Y.; Zhu, H.; Yang, Y.; Duan, T.; Sui, Y.; Han, Y.; et al. The formation and evolution of carbonate species in CO oxidation over mono-dispersed Fe on graphene. *Phys. Chem. Chem. Phys.* **2021**, *23*, 10509. [[CrossRef](#)] [[PubMed](#)]
83. Wang, J.; Wang, J.; Wang, W.; Hu, X.; Deng, Y.; Wang, H.; Wu, Y. The generation of carbon/oxygen double defects in FeP/CoP-N-C enhanced by β particles for photic driving degradation of levofloxacin. *Sep. Purif. Technol.* **2022**, *303*, 122186. [[CrossRef](#)]
84. Wang, S.; He, T.; Chen, P.; Du, A.; Ostrikov, K.; Huang, W.; Wang, L. In situ formation of oxygen vacancies achieving near-complete charge separation in planar BiVO₄ photoanodes. *Adv. Mater.* **2020**, *32*, 2001385. [[CrossRef](#)]
85. Skulason, E.; Bligaard, T.; Gudmundsdottir, S.; Studt, F.; Rossmeyl, J.; Abild-Pedersen, F.; Vegge, T.; Jonsson, H.; Norskov, J.K. A theoretical evaluation of possible transition metal electro-catalysts for N₂ reduction. *Phys. Chem. Chem. Phys.* **2012**, *14*, 1235. [[CrossRef](#)]

Disclaimer/Publisher’s Note: The statements, opinions and data contained in all publications are solely those of the individual author(s) and contributor(s) and not of MDPI and/or the editor(s). MDPI and/or the editor(s) disclaim responsibility for any injury to people or property resulting from any ideas, methods, instructions or products referred to in the content.